NASA/TM–20230004147
NESC-RP-19-01418

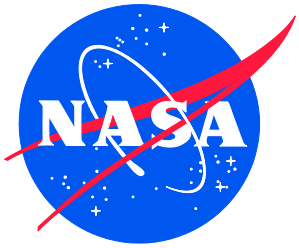

Ceramic Capacitor Grain Size Analysis Using Electron Backscatter Diffraction (EBSD)

Robert F. Hodson/NESC
Langley Research Center, Hampton, Virginia

Susana P. Douglas, Christopher M. Green
Goddard Space Flight Center, Greenbelt, Maryland

Wesley A. Tayon
Langley Research Center, Hampton, Virginia

James M. Baughman
Analytical Mechanics Associates, Hampton, Virginia

Jay A. Brusse
Science Systems and Applications, Inc., Lanham, Maryland

Henning W. Leidecker
Goddard Space Flight Center, Greenbelt, Maryland

March 2023

NASA STI Program Report Series

Since its founding, NASA has been dedicated to the advancement of aeronautics and space science. The NASA scientific and technical information (STI) program plays a key part in helping NASA maintain this important role.

The NASA STI program operates under the auspices of the Agency Chief Information Officer. It collects, organizes, provides for archiving, and disseminates NASA's STI. The NASA STI program provides access to the NTRS Registered and its public interface, the NASA Technical Reports Server, thus providing one of the largest collections of aeronautical and space science STI in the world. Results are published in both non-NASA channels and by NASA in the NASA STI Report Series, which includes the following report types:

- TECHNICAL PUBLICATION. Reports of completed research or a major significant phase of research that present the results of NASA Programs and include extensive data or theoretical analysis. Includes compilations of significant scientific and technical data and information deemed to be of continuing reference value. NASA counterpart of peer-reviewed formal professional papers but has less stringent limitations on manuscript length and extent of graphic presentations.

- TECHNICAL MEMORANDUM. Scientific and technical findings that are preliminary or of specialized interest, e.g., quick release reports, working papers, and bibliographies that contain minimal annotation. Does not contain extensive analysis.

- CONTRACTOR REPORT. Scientific and technical findings by NASA-sponsored contractors and grantees.

- CONFERENCE PUBLICATION. Collected papers from scientific and technical conferences, symposia, seminars, or other meetings sponsored or co-sponsored by NASA.

- SPECIAL PUBLICATION. Scientific, technical, or historical information from NASA programs, projects, and missions, often concerned with subjects having substantial public interest.

- TECHNICAL TRANSLATION. English-language translations of foreign scientific and technical material pertinent to NASA's mission.

Specialized services also include organizing and publishing research results, distributing specialized research announcements and feeds, providing information desk and personal search support, and enabling data exchange services.

For more information about the NASA STI program, see the following:

- Access the NASA STI program home page at http://www.sti.nasa.gov

- Help desk contact information:

https://www.sti.nasa.gov/sti-contact-form/
and select the "General" help request type.

NASA/TM–20230004147
NESC-RP-19-01418

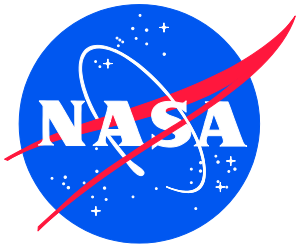

Ceramic Capacitor Grain Size Analysis Using Electron Backscatter Diffraction (EBSD)

Robert F. Hodson/NESC
Langley Research Center, Hampton, Virginia

Susana P. Douglas, Christopher M. Green
Goddard Space Flight Center, Greenbelt, Maryland

Wesley A. Tayon
Langley Research Center, Hampton, Virginia

James M. Baughman
Analytical Mechanics Associates, Hampton, Virginia

Jay A. Brusse
Science Systems and Applications, Inc., Lanham, Maryland

Henning W. Leidecker
Goddard Space Flight Center, Greenbelt, Maryland

National Aeronautics and
Space Administration

Langley Research Center
Hampton, Virginia 23681-2199

March 2023

The use of trademarks or names of manufacturers in the report is for accurate reporting and does not constitute an official endorsement, either expressed or implied, of such products or manufacturers by the National Aeronautics and Space Administration.

Available from:

NASA STI Program / Mail Stop 148
NASA Langley Research Center
Hampton, VA 23681-2199
Fax: 757-864-6500

NASA Engineering and Safety Center
Technical Assessment Report

Ceramic Capacitor Grain Size Analysis Using Electron Backscatter Diffraction (EBSD)

NESC TI-19-01418

NESC Lead: Dr. Robert F. Hodson

Technical Lead: Ms. Susana P. Douglas

February 16, 2023

Report Approval and Revision History

NOTE: This document was approved at the February 16, 2023, NRB.

Approved: TIMMY WILSON Digitally signed by TIMMY WILSON Date: 2023.03.01 10:29:13 -05'00' _____

NESC Director

Version	Description of Revision	Office of Primary Responsibility	Effective Date
1.0	Initial Release	Dr. Robert F. Hodson, NASA Technical Fellow for Avionics, LaRC	2/16/2023

Table of Contents

List of Figures

List of Tables

Technical Assessment Report

1.0 Notification and Authorization

A study on the existing analysis tools available to evaluate ceramic capacitor microstructure and produce accurate and repeatable grain size measurements and distribution data was requested by NASA Goddard Space Flight Center (GSFC) Safety and Mission Assurance Directorate, and the Electrical, Electronic, Electromechanical (EEE) Parts, Photonics, and Assembly Associate Branch Head. The results of this initial study were used to determine the necessity for a new tool development to perform this analysis. The tool development enabled grain size distributions and potential relation to capacitor reliability, which would benefit NASA and the overall space community when investigating capacitor failure root causes.

The NESC Lead for this study was Dr. Robert Hodson, NASA Avionics Technical Fellow, with support from the current Technical Lead, Susana Douglas, Acting NASA Electronic Parts Manager. The key stakeholders for this study included NASA flight programs, NASA EEE Parts Community of Practice, NASA Electronic Parts and Packaging Program (NEPP), and NASA Center EEE Parts Branches and Analysis Laboratories.

2.0 Signatures

Submitted by:

ROBERT HODSON — Digitally signed by ROBERT HODSON Date: 2023.03.01 08:05:48 -05'00'

Dr. Robert F. Hodson Date

Significant Contributors:

Susana Douglas — Digitally signed by Susana Douglas Date: 2023.02.28 17:36:45 -05'00'

Mrs. Susana P. Douglas Date

CHRISTOPHER GREEN — Digitally signed by CHRISTOPHERGREEN Date: 2023.02.28 15:55:43 -05'00'

Mr. Christopher M. Green Date

WESLEY TAYON — Digitally signed by WESLEYTAYON Date: 2023.02.28 13:53:32 -05'00'

Mr. Wesley A. Tayon Date

Electronic Concurrence received and attached

Mr. James M. Baughman Date

Jay Brusse (affiliate) — Digitally signed by Jay Brusse (affiliate) Date: 2023.02.28 12:53:36 -05'00'

Mr. Jay A. Brusse Date

Dr. Henning W. Leidecker 2/28/23

Dr. Henning W. Leidecker Date

Signatories declare the findings, observations, and NESC recommendations compiled in the report are factually based from data extracted from program/project documents, contractor reports, and open literature, and/or generated from independently conducted tests, analyses, and inspections.

3.0 Team Members

Name	Discipline	Organization
Core Team		
Dr. Robert Hodson	NESC Lead, NASA Technical Fellow for Avionics	LaRC
Susana Douglas	Technical Lead, Acting NASA Electronic Parts Manager	GSFC
Christopher Green	Assistant Chief for Technology, Former Technical Lead	GSFC
Jay Brusse	EEE Parts Engineer, Capacitor Subject Matter Expert (SME)	GSFC/SSAI
Dr. Henning Leidecker	Chief Failure Analyst for Engineering Technology	GSFC
Nilesh Shah	Destructive Physical Analysis (DPA) Engineer	GSFC
James Baughman	Research Engineer	LaRC/AMA
Wesley Tayon	Materials Research Engineer	LaRC
Consultants		
Lyudmyla Panashchenko-Ochs	EEE Parts Failure Analysis Engineer	GSFC
Dr. Alexander Teverovsky	EEE Parts Engineer, Capacitor SME	GSFC/Jacobs
Dr. Yuan Chen	Parts and Reliability Engineer	LaRC
Business Management		
Rebekah Hendricks	Program Analyst	LaRC/MTSO
Assessment Support		
Erin Moran	Technical Editor	LaRC/AMA
Linda Burgess	Planning and Control Analyst	LaRC/AMA
Melinda Meredith	Project Coordinator	LaRC/AMA

3.1 Acknowledgements

First, the NESC assessment team would like to recognize the significant contributions from the NASA Langley Research Center (LaRC) Advanced Materials and Processing Branch and Light Alloy Laboratory for providing the sample preparation and imaging and data analyses that provided the basis for the results presented in this assessment. Of equal importance were the NASA GSFC parts engineering and failure analysis specialists who paved the way for this study and continually offered guidance and supporting data that helped the assessment team to arrive at conclusions. Much gratitude is extended to the extensive support from the NASA GSFC Parts Analysis Laboratory personnel and, in particular, for Nilesh Shah's efforts, who performed cross-sectional scanning electron microscopy (SEM) images of the initial study and led to the need for the current assessment.

The NESC assessment team would like to thank John Marshall at Kyocera AVX Components Corporation and Brian Ward from Vishay Intertechnology, Incorporated, who answered NASA's request for support and provided grain size data for comparable product to the samples analyzed in this assessment, with other informative inputs. Many thanks are extended to the peer reviewers for taking the time to review and comment on the data and conclusions gathered in this report so that the NESC study can benefit from their technical expertise that are directly relevant to the science behind this study.

4.0 Executive Summary

Latent defects within multilayer ceramic capacitors (MLCCs) have resulted in multiple space mission failures, and episodic failures during system integration and test. These failures have been exhibited by increased leakage current in the capacitor, otherwise characterized as significantly reduced insulation resistance (IR). Delaminations, which are separations of the ceramic dielectric layer from the adjacent electrode plate, are intrinsic defects that can potentially propagate into cracks in the ceramic with prolonged exposure to assembly and application stresses, such as frequent cyclical variations in temperature over a wide range, and piezoelectric stresses. Cracks that bridge between two or more electrodes provide a conduit in the ceramic within which conductive films (e.g., silver dendrites) can form by electrochemical processes. These conductive films result in reduced MLCC IR over time. There are multiple factors that can lead to delamination within a capacitor, not all of which are known or fully understood. While manufacturers have developed robust and controlled manufacturing and analysis methods to remove most defective products before reaching the customer, there are physical inherent MLCC defects that cannot be screened out effectively. MLCC usage in large quantities (e.g., hundreds) on a single circuit card assembly (CCA) mandates these capacitors must be reliable to assure mission success. As such, the development of new analysis methods for assessing MLCCs is beneficial to the aerospace community.

It has been proposed by EEE subject matter experts (SMEs) that MLCC ceramic dielectric grain size should be considered a significant factor in the part reliability, and is a major factor in the ceramic mechanical fracture toughness [ref. 10]. However, most manufacturers do not directly control or monitor product grain size on mass produced product. Rather, the effects of grain size and morphology are analyzed at the initial product design phase, and the manufacturing process is controlled to produce parts with a desired grain size distribution. Due to the multiple capacitor failure occurrences in space programs, an interest existed in gathering microstructural data for investigating possible correlation of failed lots to grain size or shape. However, current methods of measuring grain size are manually intensive and can be subjective (see Appendix A). Developing an automated method of analyzing and gathering grain size data for ceramic capacitors is the primary goal of this assessment.

The use of a machine learning tool was first proposed as an automated and reproducible method for achieving an accurate grain size distribution. However, during Phase I of this assessment, the decision was made to evaluate an Electron Backscatter Diffraction (EBSD) method as an alternative to machine learning. This report explains EBSD imaging and discusses data interpretations captured from samples analyzed with this method. Five specimens were evaluated, two of which contained samples from manufacturing lots associated with instrument failures on two NASA missions, in-orbit and during ground test, on Solar Dynamics Observatory (SDO) and Landsat-7. The assessment results show that no significant grain size difference was observed in the evaluated specimens, and sufficient data were obtained to confirm this tool as an effective and automated method for imaging grain size distributions.

Recommendations have been provided to maximize proper grain identification by the EBSD tool, including upfront work to identify all secondary material phases in the sample grain structures examined, and ensuring these phases are included in the EBSD library at the time of imaging. In addition, optimization of the MLCC sample preparation techniques has been proposed to minimize unindexed EBSD map regions, with methods that include focused ion beam (FIB) milling, ion cross-section polishing, or use of other chemical agents during

mechanical polishing than those applied in this assessment. Lastly, sample "charging" impacted the image quality and grain capture rate for two samples evaluated in this study and therefore, seeking alternative strategies to improve electrical grounding of the sample has been suggested to improve data quality and the overall effectiveness of the EBSD tool.

Furthermore, while significant grain size differences were not observed among the various specimens collected in this assessment, the literature establishes a clear relationship between grain size and ceramic fracture toughness, and fracture toughness subsequently controls the propensity for ceramic cracking [ref. 9]. The conclusion was made that the absence of grain size difference between samples from the 'problem' lots and those with no evidence of subpar performance is due to 1) the failure mechanisms associated with the propensity for cracking in the select problem lots attributed to other factors in the manufacturing process completely separate from grain size or structure, and/or 2) with a sample size of only one for each lot, there is no statistical control to definitively capture problem units with propensity for cracking. A recommendation has been provided that NASA utilize the EBSD tool when investigating future lots of capacitors that show propensity for cracking, as an additional data point that can be gathered to build a library of grain size distribution data for future reference.

5.0 Assessment Plan

The original NESC assessment plan included Phases I and II as described in the following paragraphs.

Phase I involved a deep dive into existing tools and software programs available for ceramic capacitor microstructure analysis. The EBSD technique, an automated grain mapping method, was preliminarily identified as an existing analysis method that warranted investigation. Therefore, Phase I focused on examination of at least three distinct specimens using the EBSD tool and software, and determine if it could achieve the goal of accurately/repeatably assessing ceramic capacitor grain size distribution. NASA GSFC (Codes 562 and 300) obtained the MLCC samples for evaluation at a minimum.

Manufacturer	Part #	Year Of Manufacture
X	CDR35BX104BKUS	2005
X	CDR35BX104BKUS	2015
X	CDR35BX474AKSR	2010

This method was evaluated through completion of the following steps:

1) Cross-sectioned samples from each lot and prepared for EBSD inspection.
2) Performed EBSD inspection at nine sites for each capacitor, which consisted of:
    a. Selected one cross-section plane for each capacitor.
    b. Inspected three separate dielectric layers spanning from the top of capacitor to bottom of capacitor.
    c. For each dielectric layer, inspected three locations from left to right.
3) Applied statistical tools to model capacitor grain size distributions.
4) Analyzed grain size data and determined if the EBSD software tool returned sufficient information to make assessments of grain size distributions.
5) Evaluate Phase I results, and determine if assessment should proceed to Phase II.

The NESC assessment team completed the Phase I tasks, analyzing five specimens, each from manufacturing lots that included the three capacitor lots pre-selected for inspection as defined in step 1.

If the existing EBSD-based image analysis software was deemed insufficient to reliably report the grain size data output, then Phase II would continue. This phase was intended to develop a custom software algorithm/tool to perform enhanced image analysis, potentially leveraging machine learning. The software would analyze images (e.g., EBSD, atomic force microscopy, etc.) and accurately and reliably identify grain size distribution data. Phase II was not pursued due to the phase optimal results achieved for the capacitor grain size measurements and distributions.

The overall scope of this study was to identify (or develop) a tool, methodology, or process that can inspect a ceramic capacitor and consistently return repeatable grain size distribution results, with the assessment plan as described in Section 5.0. It is important to note that the development of a machine learning technique was considered as an option for this study, but only if an

existing automated tool was not available. The report explains why the EBSD analysis method for grain structure and size distribution was deemed a suitable candidate for this work.

6.0 Problem Description and Background

6.1 Basics of MLCC Materials, Processes, and Construction [ref. 11]

MLCCs are among the most-used electronic components in all electronics assemblies. A single printed wiring assembly (PWA) can contain hundreds of capacitors, and one spacecraft payload can contain tens to hundreds of thousands of capacitors. There are billions of MLCCs produced globally every day [ref. 12]. MLCCs come in a range of sizes, from a few thousandths of an inch per side up to more than an inch per side; capacitance values from picofarads to hundreds of microfarads; and voltage ratings from a few to tens of thousands of volts [ref. 12]. These apparently simple two-terminal devices belie a complex set of materials and processes that are required to produce these components. Figure 1 shows cutaway and expanded views of a typical MLCC.

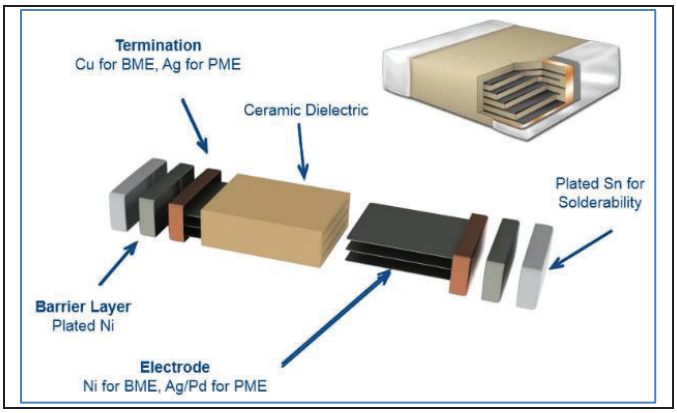

Figure 1. MLCC Cutaway and Expanded Views
Source: Kemet, a Yageo company

In its most basic form, an MLCC is produced by alternately layering controlled thicknesses of thin, electrically insulating ceramic tapes (i.e., the dielectric), or wet ceramic slurries that are subsequently dried followed by screen printing of metallic inks (i.e., the electrode plates). Each successive electrode layer is alternately offset so that it will only extend to one end of the capacitor. The ceramic dielectric formulations are most often made from proprietary formulations based on barium titanate ($BaTiO_3$) or calcium zirconate ($CaZrO_3$). There are myriad ceramic formulations with dopants, including rare earth elements like niobium (Nb), that affect the ceramic grain structure, primary and secondary material phases, and the resulting electrical MLCC performance. The electrodes are made either from palladium silver (Pd/Ag) for precious metal electrode (PME) capacitors or from nickel (Ni) for so-called base metal electrode (BME) capacitors. Ceramic powder is mixed with electrode inks to promote ceramic dielectric layer adhesion when the structure is sintered later in the process.

A dicing operation using a rotary diamond or a guillotine blade cuts the layered structure into pliable, individual chips. The chip sharp edges are softened by media tumbling (e.g., crushed walnut shells) to round the corners and edges. This multilayered structure then undergoes a controlled binder burn-out process to evolve volatiles and organic binders used in the ceramic tape, or slurry and electrode ink formulations. Next the structure is sintered using controlled

thermal profiles typically reaching peak temperatures between 1000 and 1400°C during which the structure may shrink more than 50% by volume resulting in a dense, monolithic structure. After sintering, each end of the structure is dipped into an electrically conductive (i.e., Ag or copper (Cu)) termination paste containing a frit. When fired at elevated temperatures (i.e., ~600 to 800°C), the termination frit mechanically bonds to the ceramic, and the metallic plates extending to each side are electrically connected by the conductive metals in the termination paste. Depending on the intended circuit assembly methods, the MLCC end terminations may be electroplated with a barrier layer of Ni to prevent dissolution of the underlying termination in solder, followed by a solderable final finish (e.g., tin-lead (SnPb) or Sn). For conductive epoxy mounting (e.g. using Ag or gold (Au)-filled epoxies), final finishes of electroplated Au or Pd/Ag are applied.

The outlined MLCC construction results in a single, two-terminal capacitor that comprises a multitude of individual internal capacitors connected in parallel. Depending on the target capacitance value and voltage rating, the ceramic dielectric thickness can be from sub-micron (μm) to tens of μm, and the number of dielectric layers can be from single digits to many thousands or more.

6.2 Episodic Failures of MLCCs in NASA and other Missions

Normally, MLCCs are successfully installed onto CCAs by reflow soldering or less often by hand soldering processes, or by conductive epoxy assembly methods when used inside of hybrid microcircuits (e.g., direct current/direct current (DC/DC) converters). When derated for voltage and temperature, MLCCs can perform reliably for tens of years without significant degradation. However, occasionally, problems arise when MLCCs suffer from latent failure modes involving significant IR reduction. A typical MLCC may have IR $>10^9$ ohms (Ω) at room temperature. However, if MLCC develops an internal ceramic dielectric layer crack that extends between two or more adjacent electrode plates and/or from one electrode plate to the opposing termination of the capacitor, then over time with voltage applied in the presence of a solvent capable of dissolving electrode or termination metals, an electrically conductive film may form along the crack surface due to electrochemical migration (e.g., Ag migration). As this metallic film extends along the crack surface, the MLCC's IR can drop by several orders of magnitude to resistances less than a few Ω (i.e., catastrophic short circuit).

In an KYOCERA AVX technical information bulletin titled "Cracks: The Hidden Defect" [ref. 5], the author describes a multitude of MLCC dielectric layer cracking patterns and their underlying sources including, but not limited to: thermal shock from soldering stresses; pick and place and vacuum pick up tool damage; board depanelization; board flexure; and other user handling and application stresses. Sometimes MLCC cracking failures are assigned the proximate cause of 'user abuse' during handling or assembly, especially hand soldering and 'touch up'. However, sometimes individual capacitors or significant portions of specific capacitor lots may be manufactured having intrinsic weaknesses that leave them prone to internal delaminations (i.e., the separation of a ceramic layer and an adjoining electrode plate) that can propagate with time/stress developing into cracks in the ceramic. Some causes for internal delaminations in MLCCs include high amounts of organic resins in the electrode, green-state delaminations due to lack of adhesion of the dried electrode print to the ceramic, catalytic reactions of the electrode precious metal powders with organics during binder burnout, and mismatch of the densification characteristics of the electrode and ceramic during firing [ref. 13].

One example of this latter concern has been described in GIDEP[1] Alert H6-A-19-01 [ref. 6] where two NASA missions were significantly impacted in orbit and ground testing due to MLCCs from problematic lots developing reduced IR associated with service time dependent internal delaminations and cracks. Notably, at least four other missions have been seriously affected by the same manufacturing defect, from the same facility. Failure analyses (see Figure 2) using infrared thermography, acoustic microscopy, optical microscopy, and SEM with energy dispersive x-ray spectroscopy (EDS) identified the failure site and correlation with dielectric layer cracking.

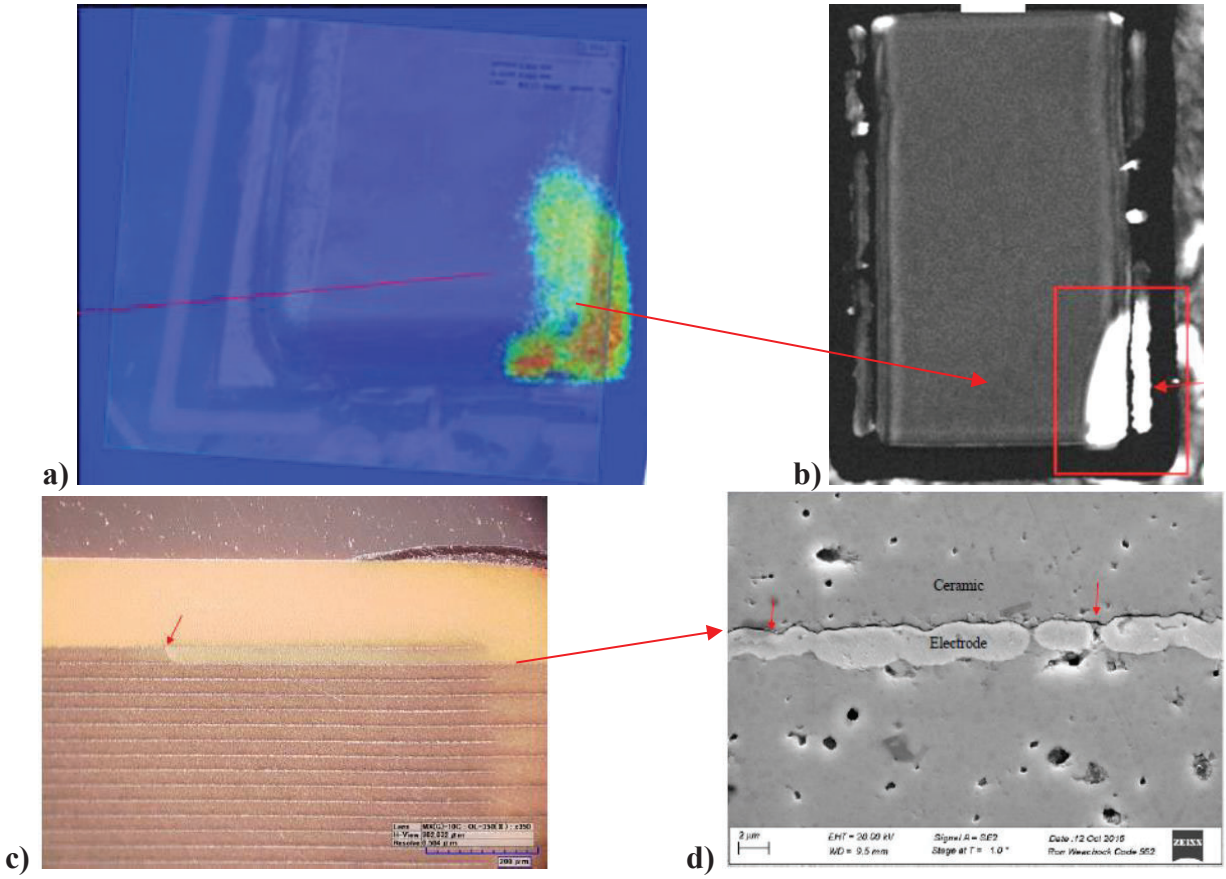

Figure 2. 2010 Manufactured MLCC with Degraded IR during Ground-based Powered Testing

Figure 2 images show:

a. Infrared image showing hot spot during powered test.
b. Acoustic microscopy image showing an internal feature in the hot spot region.
c. Cross-section showing dielectric crack extending between adjacent electrodes. A 'light' (i.e., brighter) dielectric appearance is associated with the electrode plate delaminated from the ceramic (see d).
d. SEM image showing delamination along the Pd/Ag electrode plate associated with the crack. The crack and delamination correlate with region identified by infrared and acoustic microscopy inspections (see a and b).

[1] https://www.gidep.org/

A further evaluation was performed by NASA GSFC to assess whether reflow assembly, as opposed to hand soldering, would preclude reduced IR failure modes for capacitors from one of the GIDEP problematic lots;25 MLCCs from the problematic 2010 lot were pre-screened via acoustic microscopy to document pre-existing internal features. These capacitors were then provided to their manufacturer for reflow oven assembly using their published recommended profile. As recommended by the MLCC manufacturer, an accelerated stress test was then performed using 85°C/85% relative humidity with full rated voltage applied for ~1000 hours. Room temperature IR was measured at discrete time intervals. Acoustic microscopy was repeated after printed wire board (PWB) assembly. Immediately after reflow assembly, the IR of 1 of the 25 MLCCs decreased from >10 gigaohms (GΩ) to ~3 megaohms (MΩ). During the accelerated stress test, this capacitor and five others developed significantly reduced IR dropping by 3 or more orders of magnitude (see Figure 3).

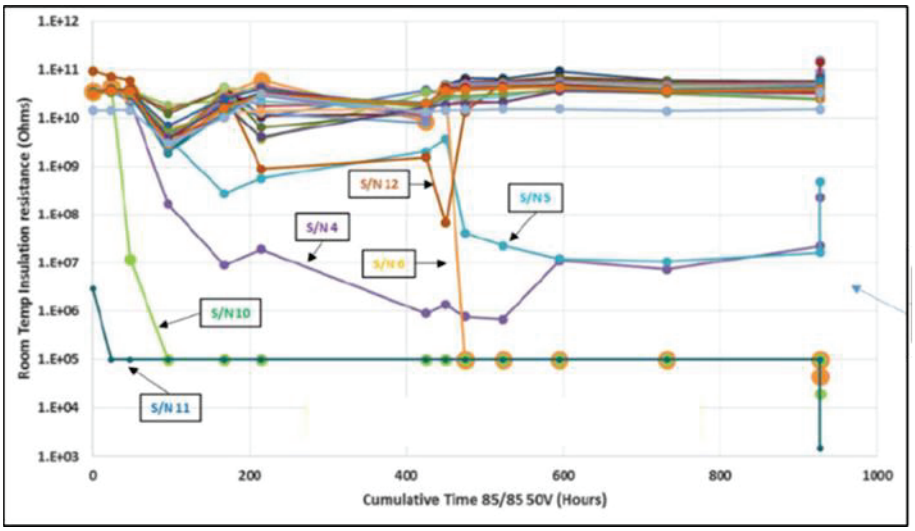

Figure 3. IR Measurement During Biased Humidity Testing on Reflow Assembled MLCCs

The failure mechanism for these six MLCCs was determined to be internal delamination propagation, cracking and electrochemical migration of Ag under bias with time. The results of this evaluation show that reflow assembly was not an effective mitigation to preclude latent failure for capacitors from this lot.

GIDEP Problem Advisory KP7-P-22-01 [ref. 7] describes similar MLCC reduced IR events with hybrid microcircuits used in reaction wheel assemblies (RWAs). In this instance, the capacitors were assembled into the hybrids using relatively benign conductive epoxy attachment processes, which the end user assembly methods were not considered to be the failure proximate cause. Rather, the subject MLCC lot had a relatively high fraction with intrinsic weaknesses making them prone to internal delaminations.

NASA and other organizations continue to experience sporadic failures in integration and test, and in the worst-case during fielded operation, despite the industry's best efforts to screen MLCC potential defects and failures through electrical and environmental testing (e.g., voltage conditioning/burn-in and acoustic imaging) [refs. 6 and 7].

6.3 Considerations of Ceramic Grain Size Distribution Effects on MLCC Reliability and Mechanical Fracture Toughness

The ceramics used in MLCCs are brittle (i.e., minimal or no measurable ductility). Ceramic material cracking propensity can be quantified using plain strain fracture toughness (K_{Ic}) under predominately linear elastic loading conditions (see Appendix A). However, the ceramics used in MLCCs are not of sufficient thickness and are constructed in a complex fashion that dramatically complicate the macro stress-strain fields and the local crack tip strain fields. There is no accepted method of measuring fracture toughness of the ceramic itself when configured as a MLCC. So measuring K_{Ic} may never be achievable on MLCC production lots without specially prepared specimens that may not represent the construction of the capacitor.

However, there is literature [refs. 1 and 2] asserting the ceramic mechanical fracture toughness or 'robustness' is related to their grain sizes (see Appendix A). The large grains in a ceramic material play a dominant role in the strength of the material. Once the inclusions are eliminated, grains from the large end of the grain size distribution become the strength-limiting flaws [ref. 14].

It is proposed to use the MLCC ceramic grain size distribution, C(d), as a proxy for K_{Ic}. If measuring C(d) were reliable, rapid, and cost effective, then the NESC assessment team could imagine using this distribution as a MLCC lot production screen. However, proof that C(d) can be correlated to MLCC ceramic fracture toughness has not been demonstrated.

The NESC assessment team incorrectly assumed the two anomalous MLCC lots had substantial differences in ceramic mechanical fracture toughness. The two lots were substantially different, but were related to Pd/Ag electrode swelling upon ingesting hydrogen. This hydrogen uptake was due to the end cap plating bath run at a high-current, followed by electrode shrinking as the hydrogen diffused out. As the electrode reduced in cross-section, it delaminated from the ceramic dielectric. Subsequently, the delamination extended along the electrode and turned sideways to form a crack that bridged to a neighboring electrode. Finally, Ag electromigrated this crack to lower the MLCC IR [ref. 8].

To study a potential correlation between MLCC ceramic fracture toughness and C(d), specimens must be obtained in which dielectric rupture is controlled by dielectric cracking, and not by internal ceramic dielectric delamination from the metal electrode.

6.4 Methods to Acquire Ceramic Grain Size Distributions

Prior to Phase I, atomic force microscopy (AFM)[2] inspection was performed on samples from MLCC lots C and E (Figure 4). Grain outlines and voids were apparent to the human eye in the AFM images. However, automated analysis tools were not available to quantify the geometries of the grains and voids. Also, internal structure within an individual grain presented challenges that made image processing algorithms ineffective to capture grain size data in an automated manner.

[2] https://en.wikipedia.org/wiki/Atomic_force_microscopy

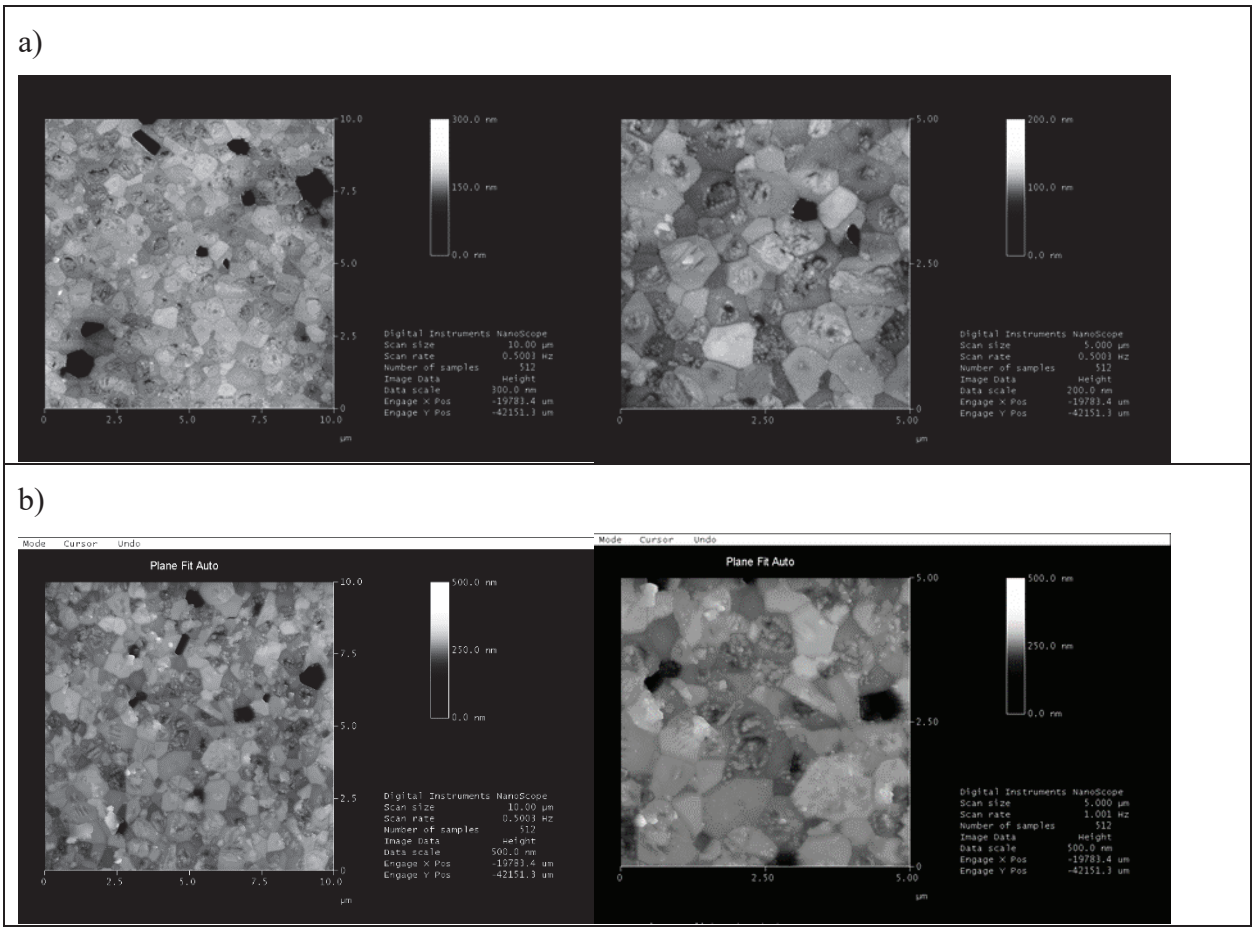

Figure 4. AFM Images of Samples from MLCC a) Lot C and b) Lot E

Subsequently, grain size data was captured both manually and by automated image processing techniques, which could be subjective producing unreliable results. Initially, image processing algorithms were applied to SEM images in an attempt to identify individual grains. Unfortunately, these algorithms were not effective. As a result, using a touch screen laptop with a stylus pen, the analyst manually traced the outline of an approximate range of 100 to 200 individual polygonal-shaped ceramic grains in each two-dimensional (2D) SEM or optical image using the ImageJ software. The software would compute the total area traced and other parameters (e.g., dimensions of best-fit circle and best-fit ellipse, etc.), and store the data into a text file for ease of export into statistical analysis tools (e.g., Microsoft Excel or SuperSmith Weibull) for distribution analysis. The time needed to manually draw the grain structure outlines yielded an estimated grain capture rate of from 0.5 to 2 grains per minute.

Figure 5 shows a comparison of the results obtained by two operators using the manual tracing of grains technique on the same SEM image from capacitor lot C. In this exercise, there was no attempt by the operators to trace all visible grains, but rather only to collect a representative sampling (e.g., more than 30 grains). Operator #1 traced the outlines of 151 grains while operator #2 traced 79 grains. Operator #1 also outlined many more grains in the range from 0.1 µm to 0.3 µm as compared to operator #2 who opted not to outline these smaller grains due to their uncertain ability to accurately identify and trace them.

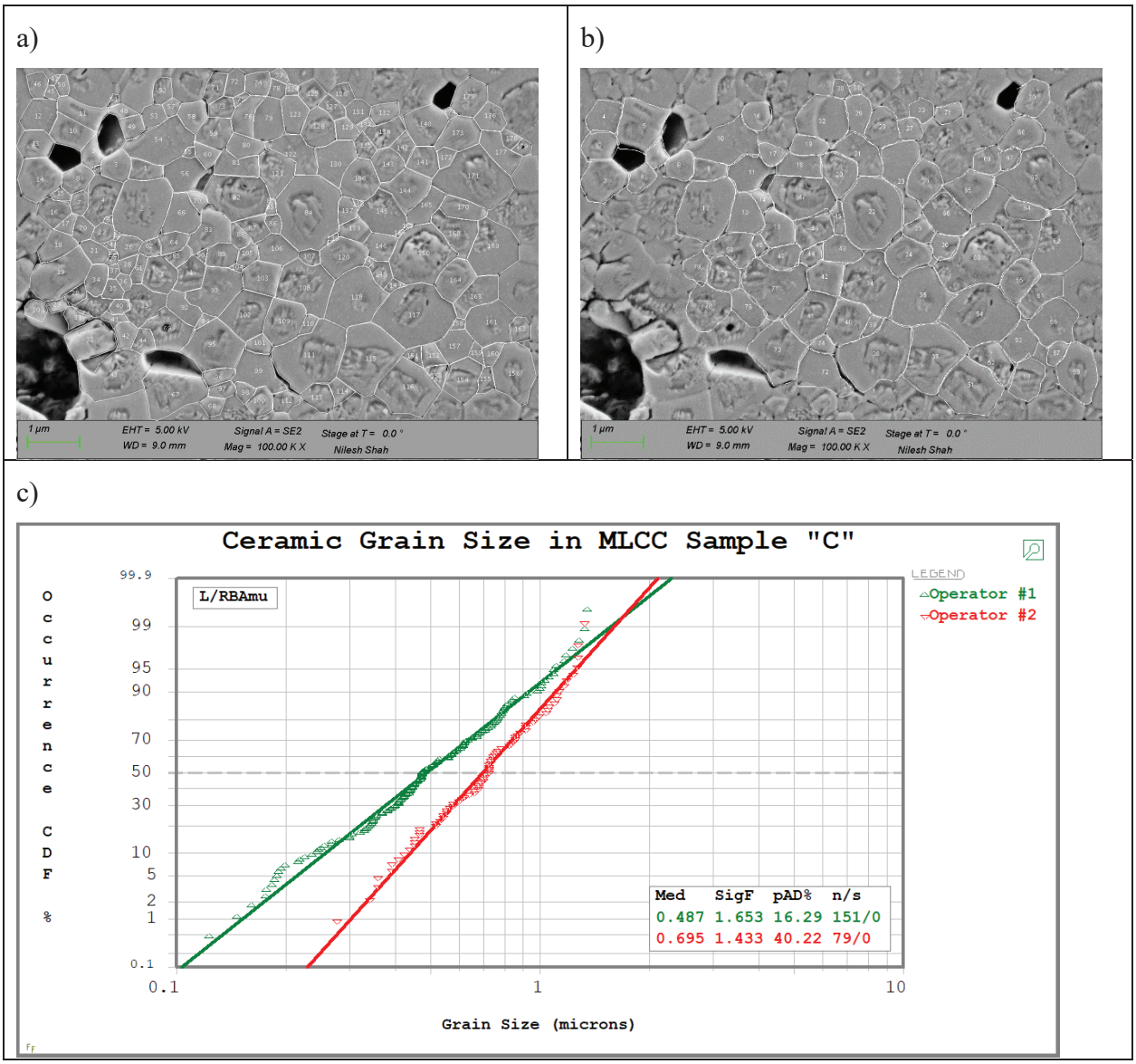

Figure 5. Manual Tracing of Grains on a SEM Image from Lot C by a) Operator #1, b) Operator #2, and c) a Comparison Grain Size Distributions obtained by Operators #1 and #2

The EBSD method of capturing grain size data used in this study circumvented this manual process. However, there is an increased imaging scan time with this method that was absent during the traditional SEM image capture. The typical EBSD image scan time for each of the nine scans on a cross-sectional sample was ~30 minutes. Using an average of 4,146 captured grains per sample from the nine scans over the total scan time yields a grain capture rate of 15.4 grains per minute. Table 1 summarizes the total time that would be required with the traditional manual method versus the EBSD technique. The sample preparation and SEM setup is assumed to be comparable between the manual and EBSD techniques. An additional consideration is the EBSD tool used has an older camera (i.e., approximately 10 years old) and a tungsten filament SEM. The EBSD camera exposure time translated to approximately 18 diffraction patterns indexed per second. With a newer technology camera and a field emission source, the EBSD scan time could likely decrease by an order of magnitude.

Table 1. Estimate of Time Required to Extract Grains in SEM Image of Ceramic Capacitor Cross-Section for the 20,730 Total Grains Identified for all Specimens in this Study

Grain Capture Method	Measurement Rate (grains/min)	# of grains	Total time (min)	Total time (hrs)
Manual Hand Trace Method	0.5	20730	41460	691.0
	1	20730	20730	345.5
	2	20730	10365	172.8
EBSD	15.4	20730	1350	22.5

The EBSD technique is a surface mapping approach to quantify grain orientation in a point-by-point grid. This technique is performed in a SEM equipped with an EBSD detector to capture the diffraction patterns generated from the interaction of the electron beam and the crystal lattice. EBSD requires a flat strain-free sample surface to generate patterns for analysis. The EBSD camera automatically acquires these patterns as the electron beam is rastered across the sample surface and indexes the patterns to determine the grain orientation. Post-processing of the grain orientation information based on user-adjustable parameters that define a grain are applied to provide grain maps enabling grain size measurement.

EBSD and optical microscopy are 2D surface imaging/mapping techniques. Inherently, grains are three-dimensional (3D) objects and most materials have a grain size variation. Sufficiently random 2D imaging will produce an acceptable representation of the materials 3D grain size distribution. Since this effect is common to manual and automated techniques as they are based on 2D images, the effective error is equal.

7.0 Analysis

The following sections summarize the experimental tools, materials, and procedures, and the corresponding captured grain size analysis results.

7.1 Description of MLCC Lots Selected for this Study

Microstructure characterization was performed on five MLCC lots. The specific lot numbers are referenced in Table 2, and have been given letter designations A through E from 2005 to 2015 date codes, and manufacturer sources X and Y. The five lots were available from GSFC project inventory and were expected to be identical or similar in parts construction. Capacitor lots C and E were associated with in-service failures and have been highlighted in gray.

All capacitors were supplied to the MIL-PRF-55681 PME performance specification, and were constructed of two or more alternating layers of $BaTiO_3$ based ceramic with proprietary additives and a metal layer acting as the electrodes.

Table 2. Capacitor Lot Information and Designation

Designation	Manufacturer	Part #	Manufacture Year
A	X	CDR35BX104BKUS	2009
B	Y	CDR35BX104BKUS	2007
C	X	CDR35BX104BKUS	2005
D	X	CDR35BX104BKUS	2015
E	X	CDR35BX474AKSR	2010

7.2 Experimental Procedure

EBSD was employed to characterize grain size and morphology. Cross-sectional samples were prepared for EBSD by potting the capacitors and then mechanically polishing using an automated micropolisher[3] with sample rotation, time, and load control. Each sample was successively polished starting with 600, 800, and 1200 grit silicon (SiC) papers, followed by a final polish with 50 nanometer (nm) colloidal silica suspension. The individual steps and details are provided in Table3. After polishing, cross-sectional samples were etched for 30 seconds with a solution of 14 mL of 35% concentration hydrochloric (HCl) acid, 4 drops of 48% concentration hydrofluoric (HF) acid, and diluted with 86 mL of deionized water applied with a cotton swab. At the conclusion of etching, samples were rinsed with acetone and dried with pressurized air.

Table 3. Mechanical Polishing Procedure for Capacitor Samples for EBSD

Step	Polishing Media	Platen Rotation	Time (min.)	Weight (gram)
1	600 grit SiC	Counter-clockwise	1.5	5
2	800 grit SiC	Counter-clockwise	1	5
3	1200 grit SiC	Counter-clockwise	1	2
4	1200 grit SiC	Clockwise	2	2
5	50 nm colloidal silica	Clockwise	5	< 2
6	50 nm colloidal silica	Counter-clockwise	5	< 2

Nine EBSD scans were collected for each of five samples, comprised of one capacitor from each of the five lots described in Table 2 above. These five samples were labeled as Samples A through E for those samples pulled from capacitor lots A through E, respectively. The nine EBSD scans were arranged in the 3 x 3 grid across the sample surface. The columns were denoted as left (L), center (C), and right (R) locations, whereas rows were numbered 1 through 3. A visual representation of the scan locations and notations are shown in Figure 6.

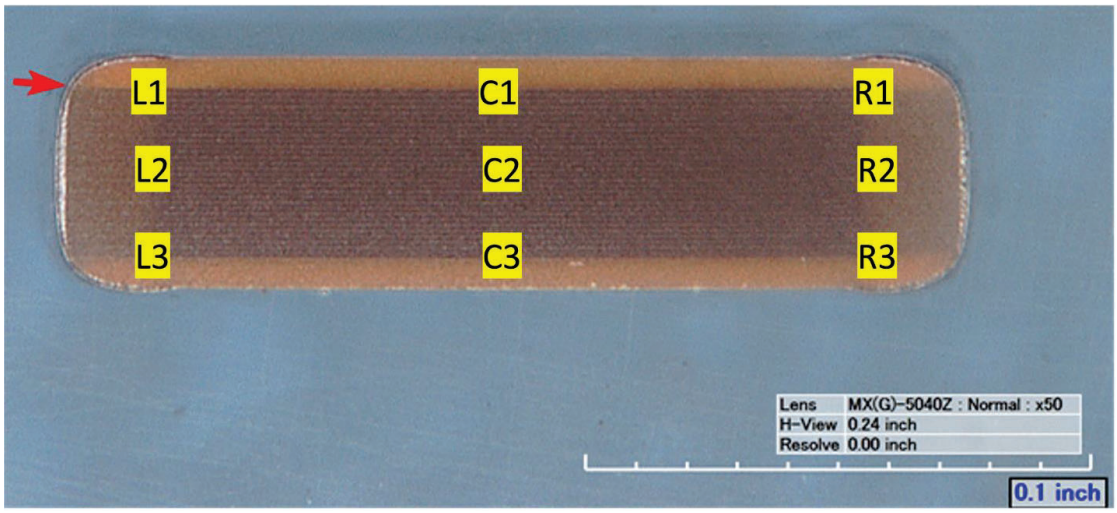

Figure 6. Example Image Depicting Approximate Location of 3 x 3 EBSD Scan Grid across the Polished MLCC Surface

[3] Allied High Tech Products, Inc. MultiPrep™ System

Each EBSD scan was collected at 5,000x magnification in a SEM (Hitachi S-3700N) at 20kV accelerating voltage and sample tilt angle of 70°. EBSD patterns were collected with an Oxford Instruments NordlysNano EBSD detector. Scans covered an area of ~18 x 18 μm^2 with a step size (pixel-to-pixel resolution) of ~0.1 µm. This scan area was selected to yield >500 grains for sufficient statistical grain size analyses [ref. 3]. Grain boundaries in the EBSD software (i.e., EDAX OIM Analysis™ v7) were defined as any pixel-to-pixel misorientation ≥15°.

The step size of ~0.1 µm was chosen to provide >5 points per grain and due to the anticipated resolution limit of the tungsten filament SEM. A grain must be fully enclosed by points with <15° misorientation and contain at least two pixels. The latter requirement in combination with the step size limit of ~0.1 µm sets a minimum resolvable/detectable grain size of ~0.2 µm.

Some areas within each scan were unindexed, which may be attributed to various factors (e.g., inconsistent sample preparation and etching, unrecognized phases, grain boundaries, or porosity). A neighbor orientation correlation filter was applied to 'cleanup' some of the unindexed regions to improve the data quality and minimize data 'noise',. The neighbor orientation correlation filter looks for points that do not match neighboring points that share a common orientation and assigns that common orientation to the unindexed point. Cleanup typically altered ~5% or less of the total scan points so as not to greatly influence or 'over-correct' the data.

Several grain size metrics have been applied to the data based on available metrics in the EBSD analysis software. These include grain area, grain diameter, and grain major and minor axes lengths. Grain area (A_i) is the number of pixels (Pi) within a grain multiplied by the step size (S) squared (see Eq. 1) [ref. 3].

$$A_i = P_i S^2 \qquad \text{Eq. 1}$$

Grain diameter (d_i) is computed from grain area assuming a circular shape (Eq. 2).

$$d_i = \sqrt{\frac{4\,A_i}{\pi}} \qquad \text{Eq. 2}$$

Grains show range of sizes and shapes. Most are nearly equiaxed polygons. It is common practice to assume a circular disc to approximate the shape of grains. Later, the team used elliptical shapes to fit the grains, but did not find a significant difference as compared to use of circles.

7.3 Results

7.3.1 EBSD Imaging

The EBSD results for samples A through E are presented in the following paragraphs. Grain maps are provided in the form of inverse pole figures (IPFs). The IPF maps plot the crystal direction that is aligned parallel to the surface normal of the EBSD scan area, and are color-coded to the stereographic triangle shown for each set of images [ref. 4]. The three principal crystal directions of <001>, <011>, and <111> are represented at the stereographic triangle corners by the red, green, and blue colors, respectively. Away from the corner regions, the colors are mixed corresponding to their relative distance from the three principal directions. The primary purpose of this map is to provide semi-quantitative visual information regarding grain orientation and size/morphology. A data table providing the average grain diameter, assuming a circular grain shape, is also presented for comparison between the nine different scan locations

for each specimen. As observed in the maps, the grain morphology is generally equiaxed, indicating that the software-applied assumption of a circular grain shape and reporting of grain sizes based on average diameter is acceptable for analysis.

IPF maps from samples A through E for the nine scan locations are presented in Figure 7, and average grain diameters for each location are provided in Table 4. Note, due to an error in data collection, the maps for sample A location R3, and sample E location L3 are smaller than the other maps. In addition, several individual EBSD scans have elongated grains which appear to be 'sheared' or 'stretched' (e.g., sample B). This is an artifact of electrical charge build up (also called beam charging) during the ~30-minute EBSD scan, resulting in the distorted appearance of the grains roughly diagonal to the rectangular scan boundaries. Since the average grain diameter is based on the grain area, there appears to be an influence of the surface charging on grain diameter measurements. A repeated scan on sample E was completed from an area that originally exhibited charging. The IPF map for this scan is provided in Figure 9 and did not exhibit charging. Figure 8 shows a comparison of the grain size distributions for the original and repeat EBSD scans for capacitor sample E region L1, and the distributions for all regions of sample E combined. The median grain size for region L1 changed from 0.727 to 0.626 µm, and the overall median grain size changed from 0.585 to 0.578 µm. While there was a change in the grain size for the re-imaged region (L1), there was little impact to the overall median grain size for sample E.

Across the five examined MLCC samples, the nine locations qualitatively appear similar in crystal orientation (i.e., color distribution based on the stereographic triangle) and grain size/morphology. The grain sizes in Table 4 quantitatively demonstrate the consistency across the nine sample locations based on average grain diameter measurements. The average grain diameter measurements ranged from 0.55 µm minimum to 0.78 µm maximum. Capacitor sample A has the smallest average grain diameter (i.e., 0.58 µm) of the five samples examined. The average grain diameter of the other four samples was approximately 0.65 µm.

The IPF maps provided in Figure 7 provide quantification of texture (i.e., preferred grain orientation) with the scanned regions. Generally, there appears to be a lower fraction of <001> oriented grains aligned with the surface normal, and a slight preference for <111> and <011> oriented grains. Overall, the texture for each MLCC sample examined qualitatively looks similar based on the IPF maps provided with subtle variations.

As texture was not part of the initial assessment scope and initial results suggest this feature is similar across all samples, texture will not be examined.

All maps display some regions that are black, which indicate areas that were not successfully indexed with the EBSD software. The area percentages of unindexed points per sample are provided in Table 6. On average, roughly 44% of the scan area was unindexed with the highest percentage occurring in sample B. Incidentally, sample B was the only sample set that originated from a different manufacturer than all other samples examined.

Figure 10 shows an example of the area fraction of unindexed regions in an EBSD image from sample A.

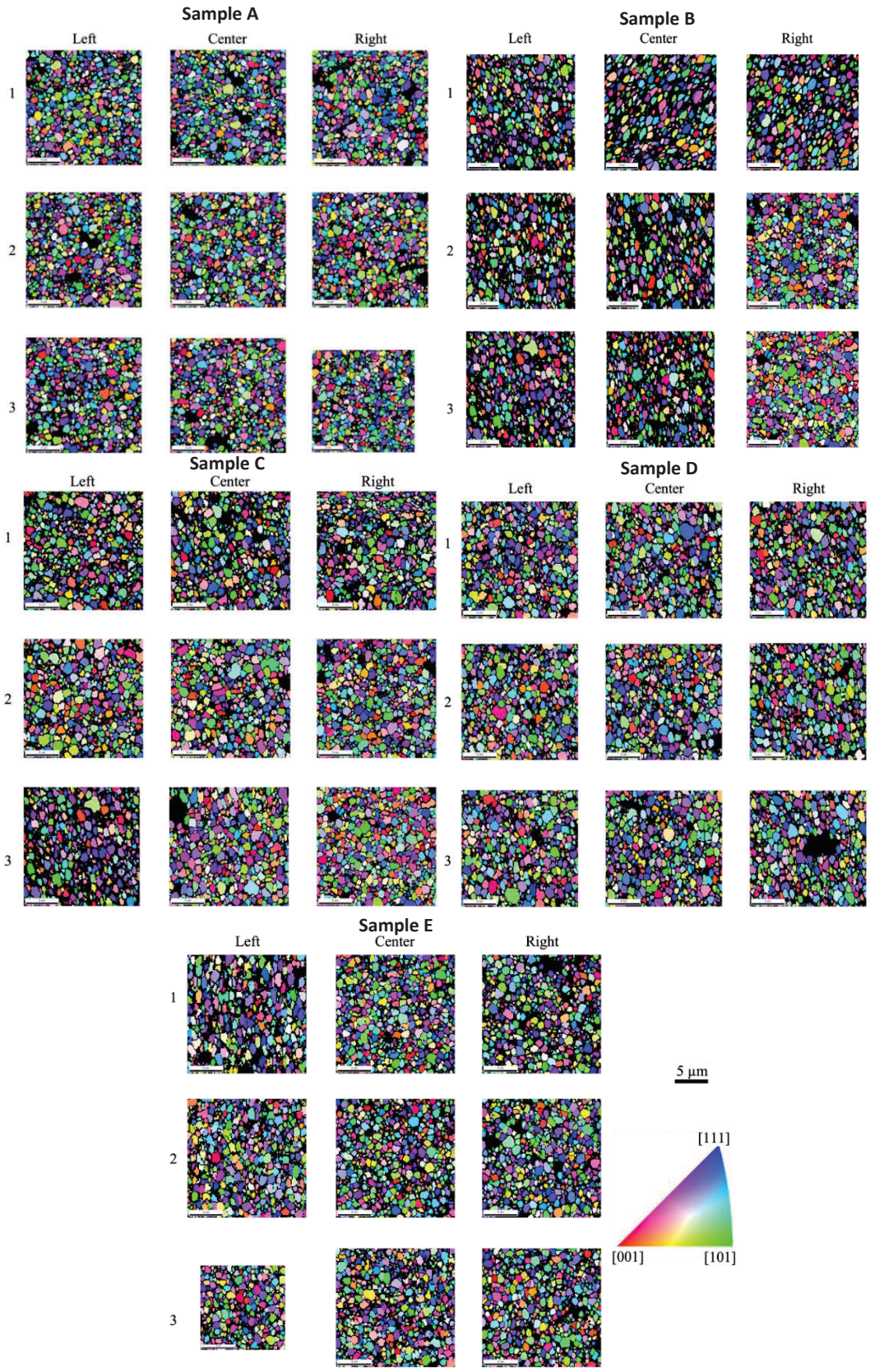

Figure 7. Inverse Pole Maps for Capacitor Samples A-E

Table 4. Average Grain Diameter (µm) for Each EBSD Scan for Capacitor Samples A-E

Location	Sample A	Sample B	Sample C	Sample D	Sample E
L1	0.59	0.62	0.62	0.63	0.78
L2	0.57	0.70	0.65	0.65	0.71
L3	0.58	0.70	0.70	0.67	0.59
C1	0.55	0.62	0.65	0.67	0.62
C2	0.59	0.75	0.68	0.69	0.59
C3	0.58	0.67	0.70	0.67	0.65
R1	0.61	0.64	0.70	0.68	0.61
R2	0.60	0.64	0.64	0.69	0.62
R3	0.58	0.63	0.63	0.70	0.60

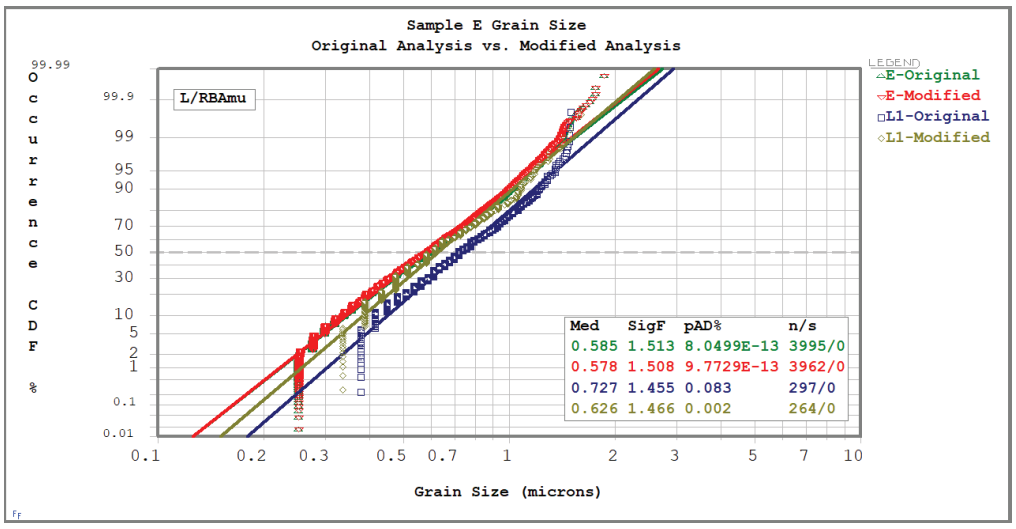

Figure 8. Effect on the Grain Size Distribution Resulting from Remeasurement of Grain Size for Sample E Region L1

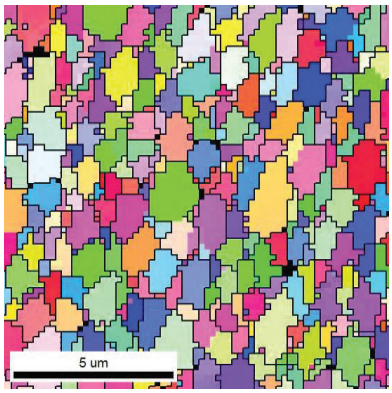

Figure 9. Repeat EBSD Scan for Capacitor Sample E

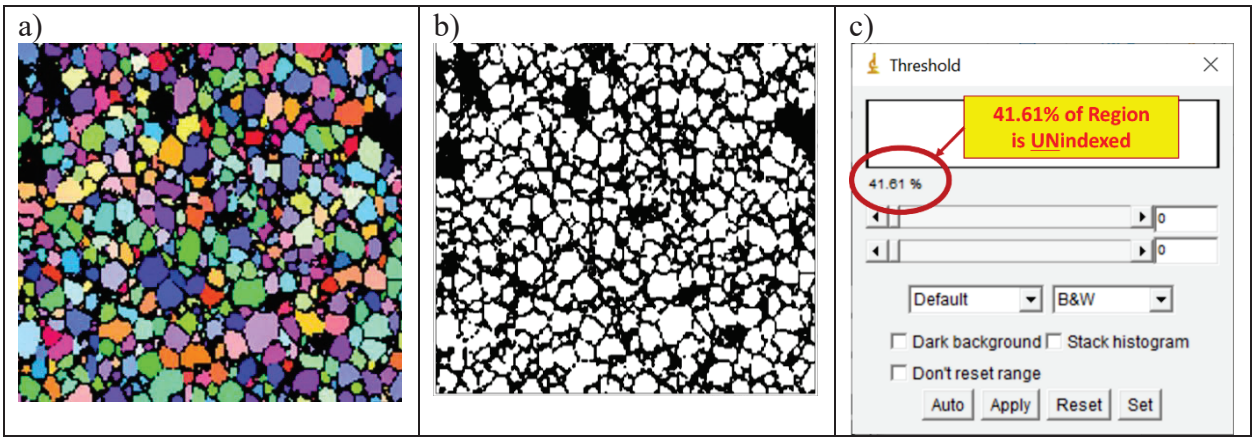

Figure 10. a) EBSD Image from Sample A Showing Indexed Regions in Color and Unindexed Regions in Black, b) ImageJ Software Conversion of EBSD Image to Binary (white and black) format, and c) ImageJ Computation of Area Fraction of Unindexed Regions during EBSD Acquisition

There are several potential explanations for the unindexed regions, which include, but are not limited to:

1) Sample preparation artifacts including grain 'pull out' during polishing and surface topographical differences that interfere with the electron beam.
2) The etchant that creates significant grain boundary relief.
3) Voids from the manufacturing process.
4) Secondary phases that were not accounted for in the indexing software.
5) EBSD software that cannot find a solution (i.e., assign a spot to a particular grain) when the beam, with spot size ~0.1 µm, overlaps two or more grains along the grain boundaries[4].

To interrogate these regions, SEM images and EDS maps were collected from the same region as an EBSD scan as shown in Figure 11. EBSD and EDS data were obtained from the boxed region in the SEM image. The band contrast map provides indication of the EBSD pattern quality with lighter shaded regions indicating 'high' quality and dark regions 'poor' quality. Correlations were drawn between the SEM image and EDS and EBSD maps to help provide understanding of the EBSD map dark regions. Below the SEM image, EBSD and EDS maps are shown: a EDS (Nb) element map, an EBSD IPF map, and an EBSD band contrast map. Note, that the sample surface was coated with gold/palladium to negate charging effects. The sample was lightly scratched to have a fiducial marker.

The majority of the EBSD map black regions appear to be voids based on correlations with 'holes' in the SEM image. The voids that appear in the SEM image and EBSD map are: 1) small, recessed areas where a grain has pulled out during polishing, or 2) manufacturing defects. The existing microscopy data are inconclusive as to which of these two sources is the dominant factor. However, the majority of the voids are consistent in size and shape with the typical grains within the capacitor material. Also, a minority of EBSD map black regions appear to correlate with Nb-rich phases based on EDS maps that are not indexed. The specific secondary phase is

[4] https://www.sciencedirect.com/science/article/pii/S0304399115001035

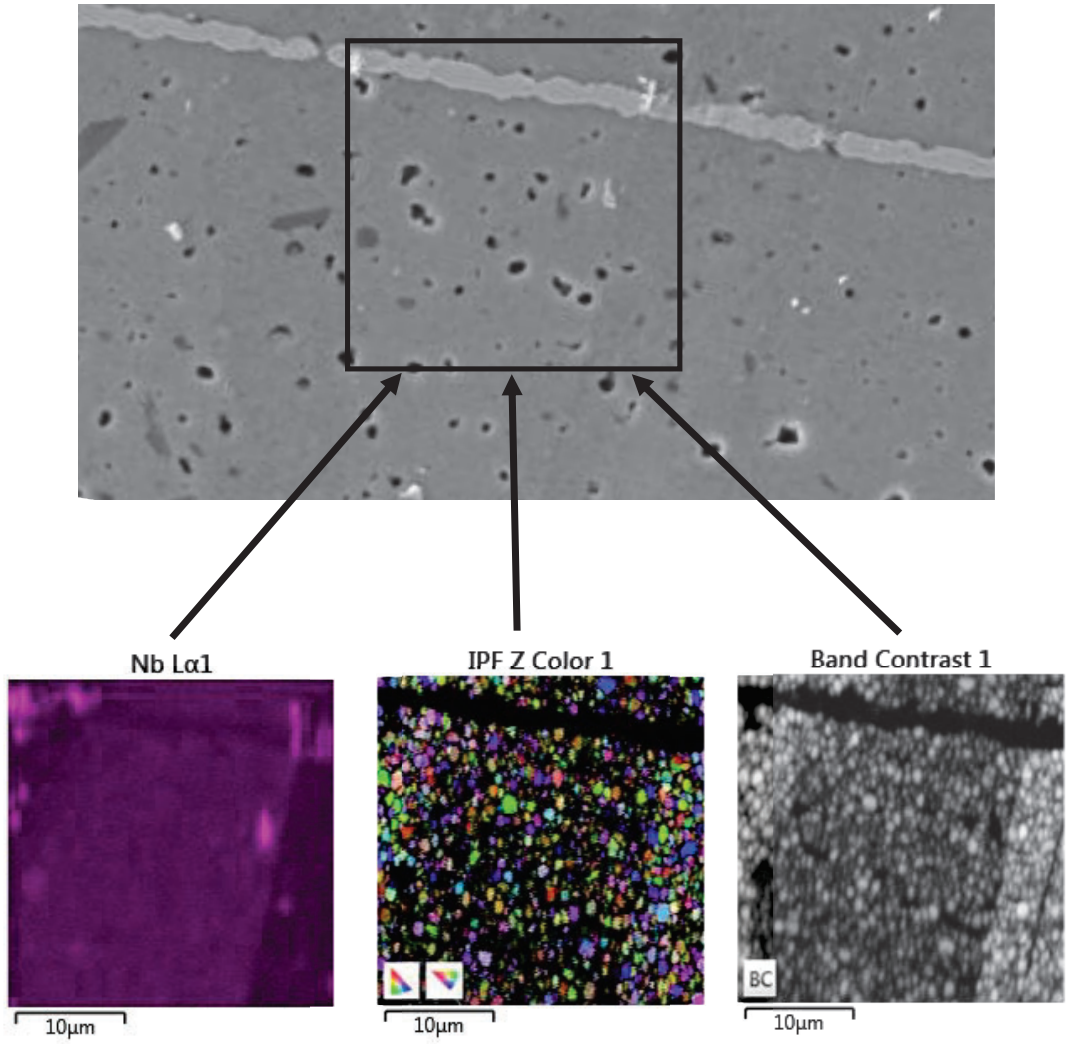

Figure 11. SEM Image with Combined Nb EDS Map and IPF and Band Contrast Maps from EBSD Corresponding to the Box Region on the Image to Assess Void-like Regions (Courtesy of the NASA GSFC Parts Analysis Laboratory)

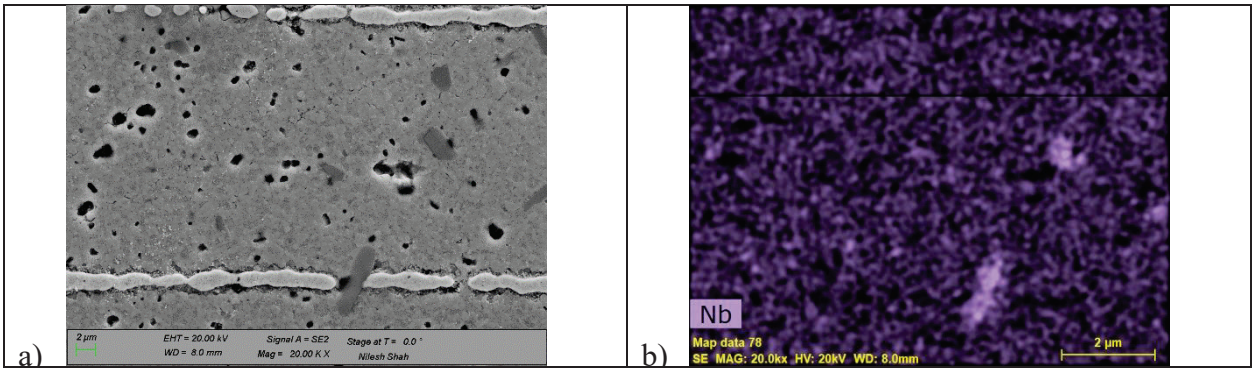

Figure 12. a) SEM Image and b) EDS Dot Map for Nb for Capacitor Sample E (Courtesy of the NASA GSFC Parts Analysis Laboratory)

unknown and therefore not indexed by the software. However, the number of these grains is small compared to the overall number of EBSD map black regions and does not account for a significant number of the black spots observed. Figures 11 and 12 provide an SEM and corresponding EDS dot map showing evidence of voids and Nb-rich secondary phases.

Figure 13 provides SEM images that were captured prior to the beginning of this NESC assessment during which manual tracing of grains was practiced. These images highlight examples of voids in the ceramic dielectric for samples from capacitor lots C and E. Using similar SEM images, an analysis of the void size distributions have been made by manually tracing the outlines of the voids using ImageJ software and computing the void area and associated void diameter. Figure 14 provides a comparison of the void size distributions for samples from capacitor lots C and E. Discussion of these plots is for a future study.

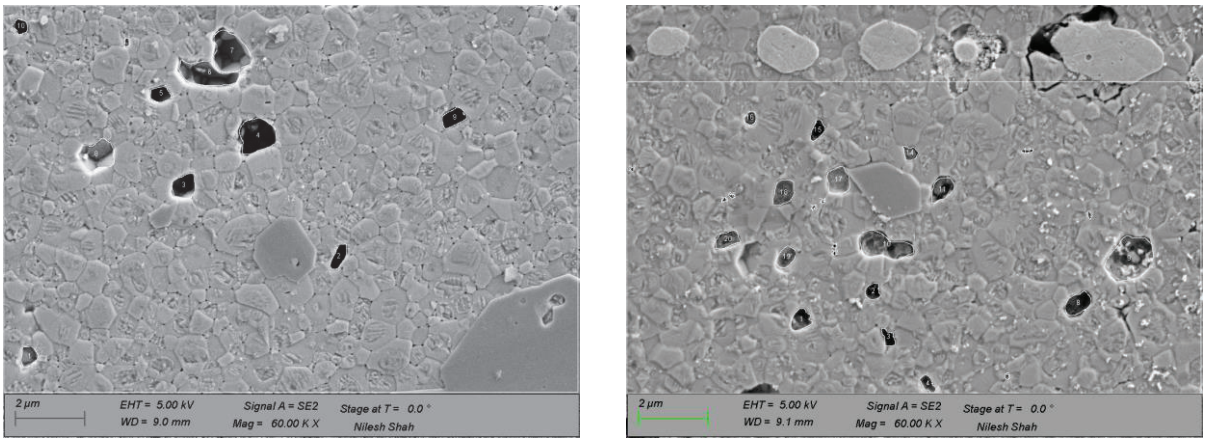

Voids in Sample from Capacitor Lot C **Voids in Sample from Capacitor Lot E**

Figure 13. SEM Images used for Measurements of Void Sizes in Ceramic Dielectric for Samples from Capacitor Lots C and E

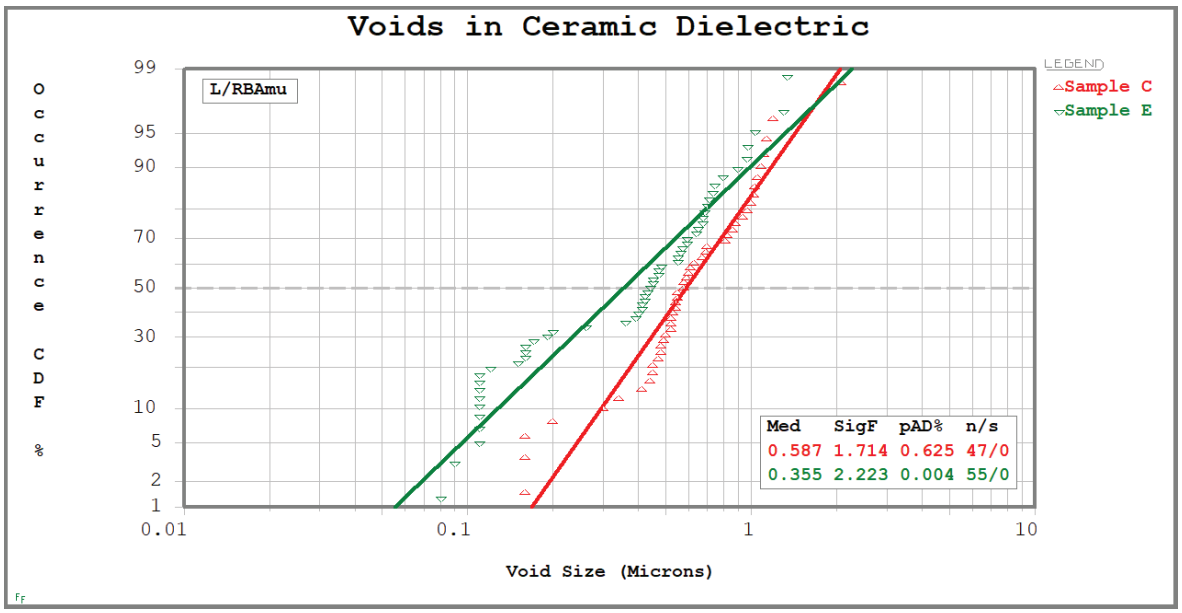

Figure 14. Void Size Distributions in Ceramic Dielectric for Samples from Capacitor Lots C and E

In summary, the five MLCC samples appear similar with respect to grain size and texture. There are subtle differences in grain size across the various samples, but are considered relatively small. To expand on the analysis with a higher level of fidelity than the average grain size measurements, additional grain size statistical analyses were performed to interrogate potential differences in the samples.

It should be noted that only one MLCC specimen per production lot was examined in this study which may not be sufficient sampling to draw conclusions about each lot.

7.3.2 Ceramic Grain Size Distribution Analysis

The ceramic grain size data was exported for analysis using Microsoft Excel and SuperSmith Weibull software tools. Table 5 provides an example of the data that was acquired for more than 20,000 grains from all five specimens combined.

Table 6 and Figure 15 provide a basic summary of the number of grains measured and the average, maximum, and standard deviation of grain size for all five specimens. As noted, there were no significant differences observed among these particular samples.

Table 7 and Figure 16 provide a comparison of grain size versus cross-section region of interest (i.e., the 3 x 3 grid locations that were measured). There was no significant difference for the distributions of grain sizes based on region of interest. Figure 17 provides a comparison of the overall grain size distributions for each of the five samples A through E, which shows no significant difference.

Grain size distributions were assessed using SuperSmith Weibull software. Figure 17 provides a comparison of samples A through E assuming a lognormal distribution and best-fit circle for grain size parameter. In this particular study there are no distinguishing features in the grain size distributions for samples C and E, pulled from the 'problematic' lots, that would separate them from the other samples analyzed. The low tail of these distributions has been clipped in the range of ~0.20 to 0.25 µm grain size threshold due to the resolution limitations described in Section 7.2.

Figure 18 provides a comparison of the grain size distributions for a sample from lot C, obtained by the manual tracing of grains on an SEM image method (operators #1 and #2) versus the EBSD method. The EBSD method acquired grain size data for ~3000 grains as compared to 151 grains and 79 grains traced manually by operators #1 and #2, respectively. The ESBD technique set a minimum grain size threshold of 0.25 µm (similar to operator #2). Accounting for the boundaries established by the three independent measurements, the three distributions appear to be more similar than distinct from one another especially with respect to grains larger than roughly 0.3 µm. One of the benefits of the EBSD technique over the manual tracing method is its orders of magnitude faster acquisition rate that enables measuring grain size for a much larger number of grains thus establishing a more detailed distribution. The EBSD technique uses crystallographic orientation to identify individual grains whereas the manual tracing technique relies heavily on human biases to interpret grain boundaries from an SEM image.

Table 5. Example of Grain Size Data Captured via EBSD

Sample ID	Region of Interest	Grain ID	Grain Perimeter (µm)	Grain Area (µm^2)	***Grain Size (µm)***
A	R3	587	2.61	0.273	***0.589***
A	R3	588	2.81	0.263	***0.578***
A	R3	589	2.01	0.182	***0.481***
A	R3	590	3.01	0.414	***0.726***
A	R3	591	3.42	0.525	***0.818***
A	R3	592	3.82	0.576	***0.856***
B	C1	1	0.96	0.032	***0.202***
B	C1	2	0.96	0.032	***0.202***
B	C1	3	1.76	0.096	***0.350***
B	C1	4	0.96	0.032	***0.202***
B	C1	5	1.6	0.096	***0.350***
B	C1	6	0.96	0.0384	***0.221***

Table 6. Statistical Summary of Ceramic Grain Size Measured via EBSD

Sample ID	StdDev Grain Size (µm)	Avg Grain Size (µm)	Max Grain Size (µm)	# of Grains	% Unindexed
A	0.25	0.59	1.89	5293	40.3
B	0.28	0.65	2.21	3268	54.8
C	0.30	0.65	2.47	4278	41.3
D	0.29	0.67	2.37	3896	42.2
E	0.27	0.64	1.86	3995	44.2
Total	*0.28*	*0.64*	*2.47*	*20730*	*44.6*

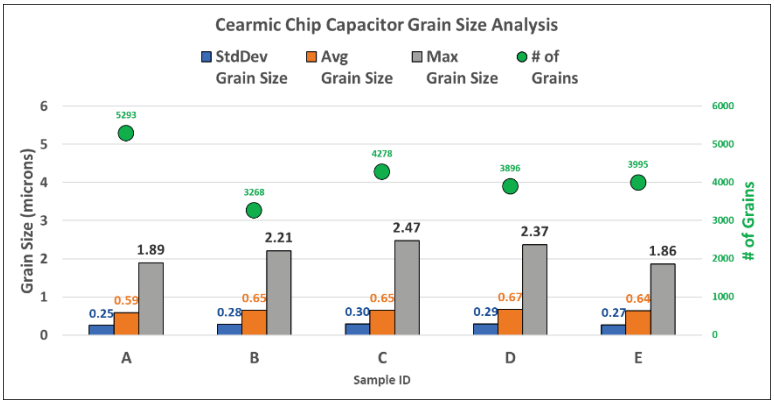

Figure 15. Statistical Summary of Ceramic Grain Size Measured via EBSD

Table 7. Grain Size Statistics versus Region of Interest for Samples A-E

Sample	Location	StdDev	Avg	Max	Count
A	L1	0.26	0.59	1.89	584
	L2	0.24	0.57	1.86	616
	L3	0.25	0.60	1.59	554
	C1	0.24	0.57	1.68	629
	C2	0.25	0.59	1.47	604
	C3	0.25	0.59	1.53	591
	R1	0.26	0.61	1.79	559
	R2	0.25	0.60	1.58	564
	R3	0.25	0.60	1.66	592
B	L1	0.27	0.62	1.62	403
	L2	0.28	0.68	1.56	333
	L3	0.28	0.68	2.21	339
	C1	0.28	0.60	1.49	390
	C2	0.30	0.75	1.67	272
	C3	0.26	0.66	1.85	334
	R1	0.30	0.63	1.94	388
	R2	0.27	0.62	1.53	412
	R3	0.29	0.64	1.51	397
C	L1	0.28	0.62	1.87	439
	L2	0.31	0.66	1.76	460
	L3	0.31	0.67	2.47	473
	C1	0.29	0.66	1.73	402
	C2	0.31	0.68	2.06	460
	C3	0.31	0.69	2.15	458
	R1	0.29	0.61	1.86	475
	R2	0.29	0.64	1.78	525
	R3	0.28	0.63	1.56	586
D	L1	0.28	0.65	2	467
	L2	0.29	0.66	2.1	456
	L3	0.32	0.67	2.35	446
	C1	0.30	0.67	2.37	428
	C2	0.28	0.67	1.64	449
	C3	0.30	0.67	1.91	435
	R1	0.29	0.68	1.97	415
	R2	0.30	0.69	1.69	404
	R3	0.30	0.70	2.01	396

Sample	Location	StdDev	Avg	Max	Count
E	L1	0.29	0.78	1.5	297
	L2	0.26	0.72	1.45	400
	L3	0.26	0.59	1.56	287
	C1	0.26	0.62	1.76	539
	C2	0.25	0.59	1.59	519
	C3	0.25	0.65	1.72	463
	R1	0.27	0.61	1.46	462
	R2	0.27	0.62	1.76	510
	R3	0.26	0.60	1.86	518

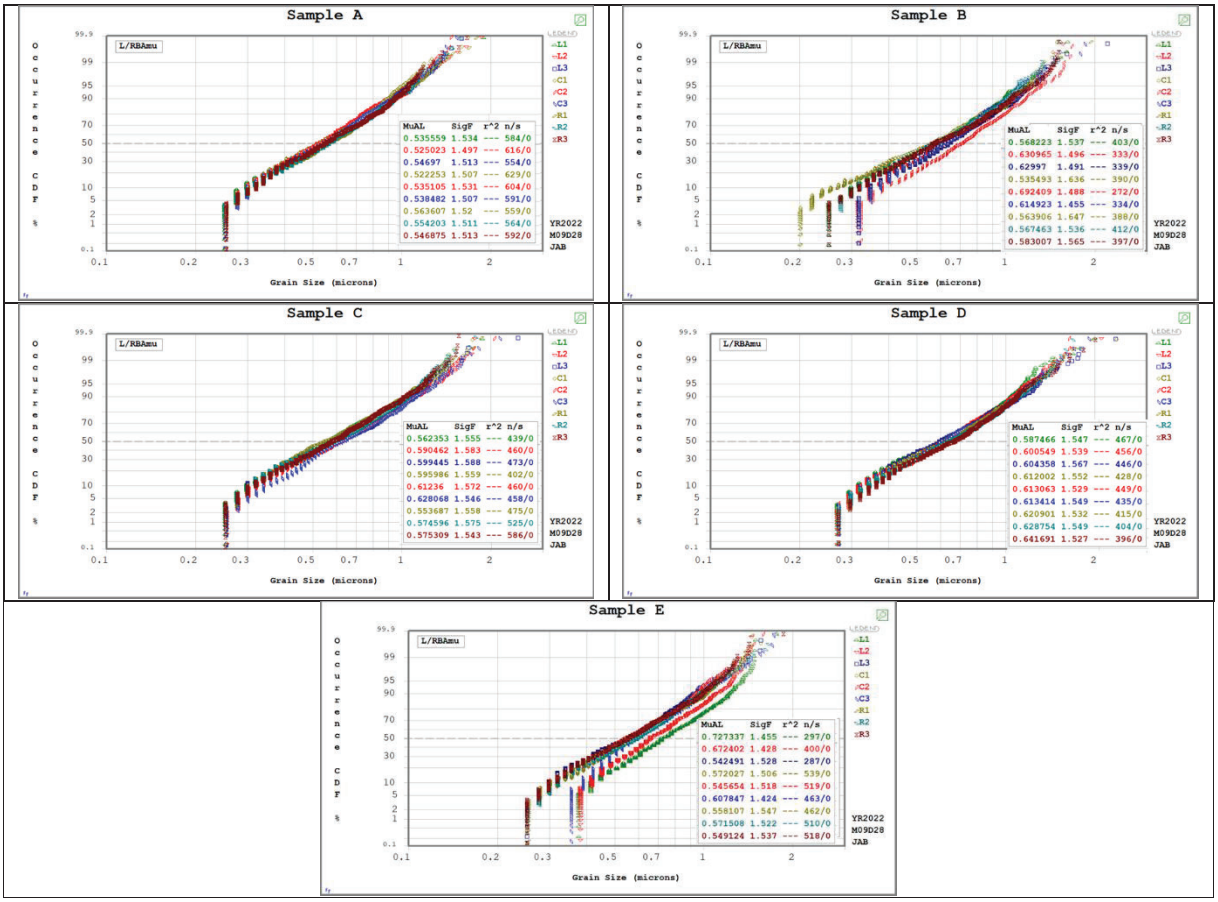

Figure 16. Grain Size versus Region of Interest for Samples A through E

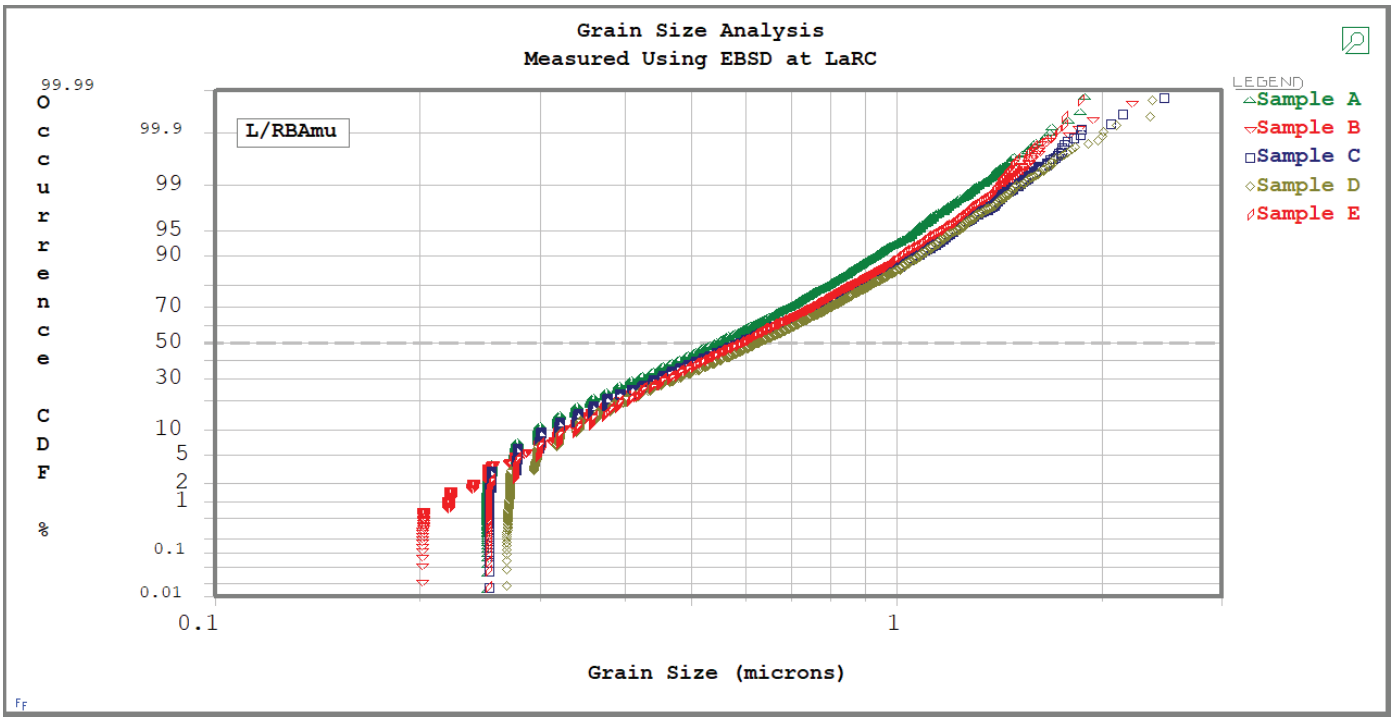

Figure 17. Lognormal Distribution Analysis of Ceramic Grain Size for Samples A through E

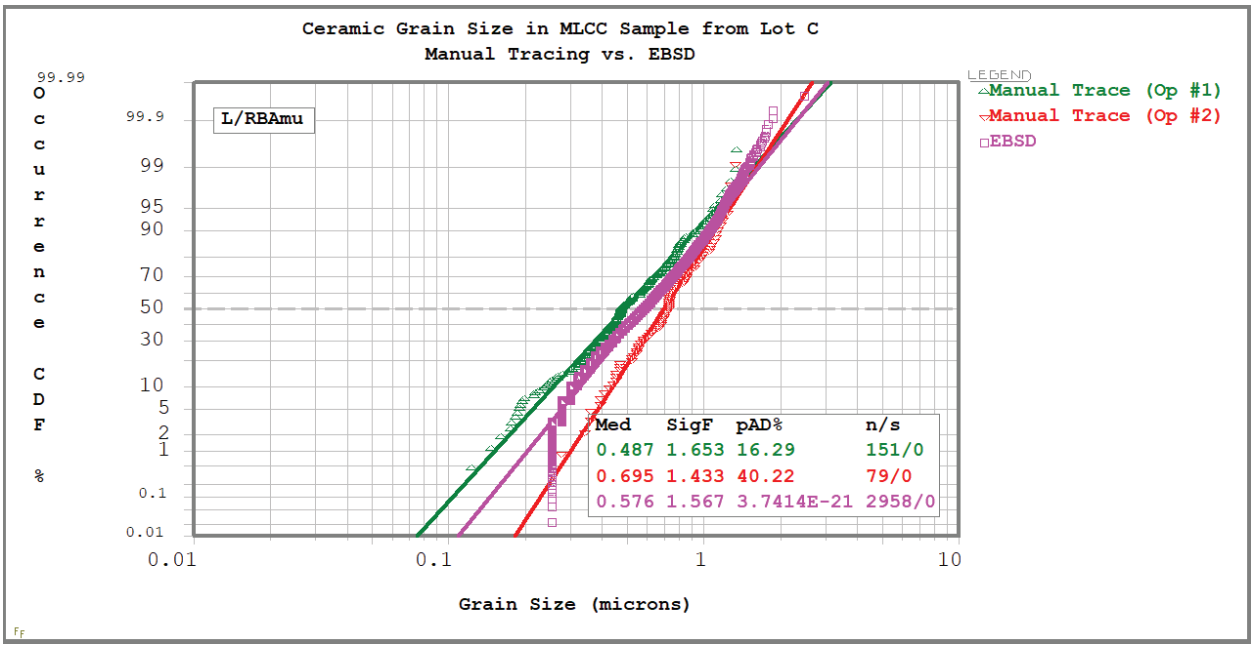

Figure 18. A Comparison of Grain Size Distributions obtained for Samples from Lot C using Both the Manual Grain Tracing Technique (2 operators) versus the Automated EBSD Technique

8.0 Findings, Observations, and NESC Recommendations

8.1 Findings

The following findings were identified during this assessment.

F-1. A method has been developed for the sample preparation of a MLCC that is suitable for subsequent analysis of ceramic dielectric grain size using EBSD techniques. However, the sample preparation techniques used in this assessment have room for improvement, per below.

- First, the current mechanical polishing procedure may have resulted in grain pull out, leading to unindexed regions.
- Second, the etchant used tended to create significant relief at grain boundaries, which may have decreased the indexing success rate in these areas.
- Lastly, the preparation routine may have to be tailored differently to allow for better indexing of secondary phases, like the unindexed Nb-containing grains referenced in the report.

F-2. EBSD is an effective tool to quantitatively acquire detailed grain structure data for ceramic capacitor dielectrics. With its built-in automation for data acquisition, the EBSD technique acquires grain size data for many hundreds to thousands of grains at a rate that is over an order of magnitude faster than prior techniques (e.g., SEM combined with manual grain size measurements).

F-3. C(d) was not a discriminating characteristic in the five MLCC production lots examined and their corresponding propensity for dielectric layer cracking or delamination. However, in this work, the team assessed one MLCC specimen per production lot which may not be sufficient sampling to draw conclusions about each lot. There is no guarantee that the specimen examined from the lots associated with on-orbit and ground-test failures was representative of the observed insulation resistance degradation failures in those lots.

F-4. Grain size distributions acquired over nine distinct regions within the five MLCC lots and associated specimens were found to be statistically homogenous (i.e., no effect of location within the sample).

F-5. Unindexed EBSD map regions caused by sample preparation method, manufacturing defects, microstructure secondary phases, and EBSD software difficulties indexing regions that overlay grain boundaries, do not account for a major portion of the microstructural region of interest.

8.2 Observation

The following observation was identified during this assessment.

O-1. Literature shows grain size and fracture toughness are related for some ceramics. However, there are no known methods of measuring fracture toughness of the ceramic material when configured as an MLCC.

8.3 NESC Recommendations

The following NESC recommendations are directed to NASA EEE Parts Community of Practice, NASA Electronic Parts and Packaging Program (NEPP), and NASA Center EEE Parts Branches and Analysis Laboratories.

R-1. Repeat C(d) measurements utilizing modern EBSD tools, ensuring the EBSD library includes all identified secondary phases, to assess higher data acquisition rates and finer resolution for sub-µm grain size MLCC ceramic dielectrics. ***(F-1, F-2, F-5)***

R-2. Optimize MLCC ceramic dielectric sample preparation techniques to minimize unindexed EBSD map regions (e.g., focused ion beam milling, ion cross-section polishing, or the use of other chemical agents during mechanical polishing). Alternative strategies to improve electrical grounding of the sample would also serve to improve data quality. ***(F-1, F-5)***

R-3. The NASA Electronic Parts and Packaging Program (NEPP) should investigate future lots of capacitors that show propensity for cracking via EBSD and grain size distribution. The literature [ref. 9] contains many references to the relationship between grain sizes and fracture toughness, and fracture toughness controls propensity for cracking. ***(F-2, F-3, F-4, O-1)***

9.0 Alternate Technical Opinion(s)

No alternate technical opinions were identified during the course of this assessment by the NESC assessment team or the NESC Review Board (NRB).

10.0 Other Deliverables

No unique hardware, software, or data packages, other than those contained in this report, were disseminated to other parties outside this assessment.

11.0 Recommendations for the NASA Lessons Learned Database

No recommendations for NASA lessons learned were identified as a result of this assessment.

12.0 Recommendations for NASA Standards, Specifications, Handbooks, and Procedures

No recommendations for NASA standards, specifications, or procedures were identified as a result of this assessment.

13.0 Definition of Terms

Finding	A relevant factual conclusion and/or issue that is within the assessment scope and that the team has rigorously based on data from their independent analyses, tests, inspections, and/or reviews of technical documentation.
Lesson Learned	Knowledge, understanding, or conclusive insight gained by experience that may benefit other current or future NASA programs and projects.

	The experience may be positive, such as a successful test or mission, or negative, as in a mishap or failure.
Observation	A noteworthy fact, issue, and/or risk, which is not directly within the assessment scope, but could generate a separate issue or concern if not addressed. Alternatively, an observation can be a positive acknowledgement of a Center/Program/Project/Organization's operational structure, tools, and/or support.
Problem	The subject of the independent technical assessment.
Recommendation	A proposed measurable stakeholder action directly supported by specific Finding(s) and/or Observation(s) that will correct or mitigate an identified issue or risk.

14.0 Acronyms and Nomenclature List

Ω	ohm
2D	Two-Dimensional
3D	Three-Dimensional
AFM	Atomic Force Microscopy
Ag	Silver
Au	Gold
BaTiO3	Barium Titanate
BME	Base Metal Electrode
CaZrO3	Calcium Zirconate
C(d)	Grain Size Distribution
Cu	Copper
DC	Direct Current
EBSD	Electron BackScatter Diffraction (Microscopy)
EDS	Energy Dispersive (X-ray) Spectroscopy
EEE	Electrical, Electronic, Electromechanical
FIB	Focused Ion Beam
GSFC	Goddard Space Flight Center
IPF	Inverse Pole Figure
IR	Insulation Resistance
HCl	Hydrochloric (acid)
HF	Hydrofluoric (acid)
LaRC	Langley Research Center
MLCC	Multilayer Ceramic Capacitor
NEPP	NASA Electronic Parts and Packaging Program
NESC	NASA Engineering and Safety Center
Ni	Nickel
Pd/Ag	Palladium Silver
PME	Precious Metal Electrode
PWA	Printed Wiring Assembly
RWA	Reaction Wheel Assembly
SDO	Solar Dynamics Observatory
SEM	Scanning Electron Microscope

SiC	Silicon
SME	Subject Matter Expert
SnPb	Tin-Lead

15.0 References

1. Liu, D., *"A General Reliability Model for Ni-BaTiO3-Based Multilayer Ceramic Capacitors", CARTS International, April 2014. https://nepp.nasa.gov/files/25994/2014-562-Liu-Final-web-CARTS2014-paper-TiO3BME-TN14691.pdf.*
2. *NASA GSFC S-311-P-838, "Capacitor, Ceramic, Multilayer Chip, Base-Metal Electrodes, Space Applications," https://nepp.nasa.gov/files/30348/S-311-P-838B.pdf.*
3. ASTM E2627 - 10. Standard Practice for Determining Average Grain Size Using Electron Backscatter Diffraction (EBSD) in Fully Recrystallized Polycrystalline Materials. ASTM International, West Conshohocken, PA. 2010.
4. Schwartz, Adam J., et al., eds. Electron backscatter diffraction in materials science. Vol. 2. New York: Springer, 2009.
5. Maxwell, J., *"Cracks: The Hidden Defect," 38th Electronics Components Conference 1988., Proceedings., 1988, pp. 376-384, doi: 10.1109/ECC.1988.12620.*
6. H6-A-19-01, Multilayer Ceramic Chip Capacitors (MLCCs) with Internal Delaminations and Cracks Leading to Reduced Insulation Resistance Failure Modes in Service, October 22, 2018, AVX Corporation.
7. KP7-P-22-01A, Multilayer Ceramic Capacitors with External Cracks Resulting in Non-Compliant Hybrid Microelectronic Devices, April 15, 2022, Kyocera AVX Components Corporation.
8. Alexander T.'s "Cracking of MLCCs" NEPP report as reference: https://nepp.nasa.gov/files/29931/NEPP-BOK-2018-Teverovsky-Paper-NEPPWeb-BOK-Cracking-MLCC-TN65668.pdf.
9. Rice, Roy W., *"Mechanical Properties of Ceramics and Composites, Grain and Particle Effects, 696 pp.*
10. Liu, D., *How to Characterize the Reliability of Ceramic Capacitors with Base-Metal Electrodes (BMEs), 3/1/2015.* URL https://nepp.nasa.gov/files/26548/2015-562-Liu-Final-Pres-NEPPweb-CMSE2015-TN22757.pdf.
11. "Multilayer Ceramic Capacitors Materials and Manufacture", Manfred Khan, Kyocera AVX components (circa 1981) https://www.kyocera-avx.com/docs/techinfo/CeramicCapacitors/mlcmat.pdf.
12. "Ceramic Products Update", Wilson Hayworth, Yageo Kemet, July 27, 2022.
13. Pepin, J.G., Borland, W., O'Callaghan, P. and Young, R.J.S. (1989), Electrode-Based Causes of Delaminations in Multilayer Ceramic Capacitors. Journal of the American Ceramic Society, 72: 2287-2291. https://doi.org/10.1111/j.1151-2916.1989.tb06076.x.
14. George Quinn has published the third edition of his freely-downloadable "NIST Recommended Practice Guide: Fractography of Ceramics and Glasses", page 6-84: https://nvlpubs.nist.gov/nistpubs/specialpublications/NIST.SP.960-16e3.pdf

Appendices

A. Fracture Toughness of Ceramics and the Role of Grain Size

Appendix A. Fracture Toughness of Ceramics and the Role of Grain Size

Fracture Toughness of Ceramics and the Role of Grain Size

Henning Leidecker
Code 560, GSFC
Henning.W.Leidecker@NASA.gov

February 13, 2023

1 Introduction

Multi-Layer Ceramic Capacitors (MLCC) are widely used in electrical circuits. There are presently about a trillion (10^{12}) produced each year. A typical NASA spacecraft uses thousands, and some use hundreds of thousands. Hence, their reliability is important. The ceramic dielectric is brittle, and so a common failure mechanism is for the ceramic to crack under stress, which can result in a change in capacitance, or even an electrical short or open.

The resistance of multilayer ceramic capacitors to cracking varies with the choice of ceramic used for the dielectric. Experience has shown that C0G dielectric does not crack as readily as X7R dielectric under the same applied stresses, and that X7R does not crack as readily as do Z5U & Y5V dielectrics.

One study of this is the doctoral dissertation by M. Keimasi.[1] Dr. Keimasi describes testing that was carried out on size 1812 MLCC capacitors incorporating C0G and X7R dielectrics – 96 with each dielectric – that were mounted on boards which were increasingly flexed up to a level of about 13,000 micro strains (a strain of 1.3%). **None of the capacitors with C0G dielectric showed evidence of cracking even at the maximum strain level; however, 94 out of 96 capacitors with X7R dielectric cracked, and failed.** One way to understand this is in terms of *fracture toughness*, which is a material constant that measures the resistance a material offers to the extension of a crack.

[1] *FLEX CRACKING AND TEMPERATURE-HUMIDITY-BIAS EFFECTS ON RELIABILITY OF MULTILAYER CERAMIC CAPACITORS* by Mohammadreza Keimasi, 2007: https://drum.lib.umd.edu/bitstream/handle/1903/4257/umi-umd-4115.pdf?sequence=1&isAllowed=y

C. R. Koripella[2] has reported measurements of the fracture toughness for C0G, X7R, and Z5U: see Table 1. Also, S. W. Freiman, et al. reports[3] that the fracture toughness of $BaTiO_3$ is 1.05 MPa$\cdot\sqrt{\text{m}}$.

Table 1: Values of the fracture toughness K_{Ic} of three ceramics used as dielectrics in MLCC.

Ceramic:	K_{Ic} (MPa$\cdot\sqrt{\text{m}}$) without electrodes	K_{Ic} (MPa$\cdot\sqrt{\text{m}}$) with electrodes
C0G	1.07 ± 0.15	1.50 ± 0.13
X7R	0.81 ± 0.09	1.03 ± 0.15
Z5U	0.81 ± 0.10	1.01 ± 0.17

Another study is by B. Rawal, et al., who report thermal shock results for size 1206 MLCC using two examples of X7R dielectic with distinct fracture toughness.[4] Fifty examples of each were exposed to thermal shock. For X7R with a fracture toughness of 1.3 MPa$\cdot\sqrt{\text{m}}$, there were 0 failures out of the 50 units for a failure rate of 0%. For X7R with a fracture toughness of 0.9 MPa$\cdot\sqrt{\text{m}}$, there were 37 failures out of the 50 units for a failure rate of 74%.

Both results are consistent, and suggests that increasing the fracture toughness K_{Ic} of the ceramic by 20% to 50% might dramatically lower the frequency of cracking under bending stresses!

MLCCs with C0G dielectric (EIA class I) are substantially more expensive than MLCCs using X7R, and have substantially lower available values for maximum capacitance. So we will not switch entirely to the use of C0G-based MLCCs.

But this demonstrated dramatically large difference in cracking propensity between C0G and X7R does suggest that we attend to the fracture toughness of X7R. It suggests that we should be aware of any variations in the fracture toughness of X7R from lot to lot during production, or perhaps even within a lot. If there are variations, then we might prefer to purchase lots, or even individual units, with higher values of fracture toughness, and avoid those with lower values, unless other factors intrude.

After decades of work, we can now reliably measure the fracture toughness of specimens of many ceramic materials when prepared as homogeneous beams with flat polished sides; however, no one has demonstrated the ability to easily measure the fracture toughness of the ceramic component of MLCCs. Indeed, their small size and their complicated structure (which contain many metal electrodes and also multi-layer wraparound end terminations)

[2] "Mechanical Properties of Ceramic Capacitors", Kemet TechTopics, September 1991. Vol. 1, No. 5. https://citeseerx.ist.psu.edu/document?repid=rep1&type=pdf&doi=b2e771915750942186e0be77d69611fb33985a79

[3] "Slow Crack Growth in Polycrystalline Ceramics", *Fracture Mechanics of Ceramics*, Vol. 2, pages 659 to 676. (1974).

[4] *PARAMETERS IMPORTANT FOR SURFACE MOUNT APPLICATIONS OF MULTILAYER CERAMIC CAPACITORS* by Bharat S. Rawal, Jumar Krishnamani, and John Maxwell, **Technical Information**, AVX Corporation.

make such measurements on these objects highly difficult. (We see evidence of this in Koripella's values in Table 1: the fracture toughness K_{Ic} is a material constant of the ceramic, and cannot depend upon whether there are electrodes present. Clearly, the method he used to extract the fracture toughness from the data did not correctly account for the constraints imposed by the electrodes.)

There is a well-established correspondence between fracture toughness and grain size for homogeneous ceramics, and this suggests measurement of grain size of the ceramic component of a production lot of MLCCs as a proxy for fracture toughness.

The ceramics used in MLCCs show a wide range of grain sizes and shapes; however, most grains have shapes that are roughly equiaxial, and so, for simplicity, we approximate the shapes as disks and approximate the size of a grain as the diameter d of a disk having the same area A as the grain: $d = \sqrt{4A/\pi}$. Many studies of grains find that the distribution of sizes (diameters) is log-normal, and we confirm that this is a useful model in this work.

Actually, grains form a 3D structure, while conveniently available images are 2D cross-sections. The word *stereology* was defined in 1961 as 'the spatial interpretation of sections', and presents methods for inferring 3D statistics from 2D cross-sections. In this Appendix, we will work with 2D images, and comment on their relation to 3D structures in a separate appendix.

2 Ceramics: definitions, and some history

A ceramic is any of the various hard, brittle, heat-resistant and corrosion-resistant materials made by shaping and then firing at a high temperature; a ceramic is an inorganic, nonmetallic material. The earliest ceramics were figurines and pots made from clay, either by itself, or mixed with other materials like silica, and then hardened and sintered in fire. Archeologists have found a ceramic statuette of a woman (the *Venus of Dolní Věstonice*) dating to about 28,000 BC from a settlement near Brno in the Czech Republic. Ceramic pottery becomes common since roughly ten thousand years ago. The word *ceramic* comes from the Greek word κεραμικός, "of pottery" or "for pottery", from κέραμος, *potter's clay*, *tile*, *pottery*. The earliest known mention of the root "ceram-" is the Mycenaean Greek ke-ra-me-we, *workers of ceramic*, written about 1,400 BC to about 1,200 BC in the Linear B syllabic script that was used for writing Mycenaean Greek, which is the earliest known form of Greek.

Modern ceramics include a wide range of materials, ancient ones as well as ones recently developed by advanced ceramic engineering. Nearly all of the elements, with nearly all types of atomic-level bonding, have now been made into ceramics, and these have been formed with all levels of crystallinity from single crystal to completely amorphous such as glasses. Some ceramics experts do not regard amorphous materials, such as glasses, to be ceramics, while other ceramics experts do. Heat treatments can convert some glasses into a semi-crystalline material that everyone calls *glass-ceramics*. With such a large range of possible options for the composition and structure, the category of ceramic materials is vast, and

there are no precise values for the attributes of ceramics materials as a whole. Still, the norm is for high melting temperatures (ranging from 1,000°C to 1,600°C), low electrical conductivity, high modulus of elasticity, high strength in compression but low strength in shear, low ductility (i. e., high brittleness), high hardness, low fracture toughness, and high chemical resistance to both acidic and caustic environments. There are exceptions to each of these attributes. Many composites, such as matrices reinforced with fiberglass or carbon fibers, are not considered to be part of the ceramic family, even though containing ceramic materials.

3 Ceramics: mechanical properties

The physical properties of any ceramic object are a direct result of its hierarchy of structures, ranging from atomic arrangements to grain structures to its all-over shape. Solid-state chemistry and solid-state physics reveal the fundamental relations between properties such as localized density variations, grain size distribution, and types of porosity, to ceramic properties including mechanical strength, dielectric parameters, and optical properties. The microstructure includes the distribution of sizes of grains of the primary phase (and of any secondary phases and tertiary phases, etc., if present), pores, boundaries of the grains of all the types of phases including pores, structural defects, and micro-cracks. The microstructure includes any micro-indentations made during machining and handling and hardness testing. Most bulk mechanical, optical, thermal, electrical, and magnetic properties are significantly affected by the observed microstructure. The microstructure is controlled by the fabrication method, and subsequent processing conditions. The root cause of many ceramic ruptures becomes evident upon inspection of the fractured surfaces, as explored by *Fractography*.[5]

4 Linear Elastic Behaviors and Plastic Behaviors

It can happen that the strain is a function of the applied stress; that is, whenever the applied stress returns to a given value, then the strain also immediately returns to the corresponding value, again and again: this is the defining condition of *elastic behavior*, and it is a useful description of the relationship between small applied stresses and small deformations for many materials. When the strain is not a function of applied stress, but depends on the history of that stress, so that there is permanent deformation of the specimen, then the behavior is *plastic*: this is a common behavior for many materials when subjected to large applied stresses.

[5]Two excellent books are:
George D. Quinn, **Fractography of Ceramics and Glasses** by George D. Quinn: NIST Recommended Practice Guide, Special Publication 960-16e2; Third Edition, September 2020.
V. D. Fréchette, **Failure Analysis of Brittle Materials**, Advances in Ceramics, Vol. 28, American Ceramic Society, Westerville, OH, 1990.

It can happen that the strain is a linear function of the applied stress: this is the defining condition of *linear elastic behavior*. Robert Hooke noted this behavior for metals shaped as springs in 1678 (but claims he knew it in 1660), saying *ut tensio, sic vis* : *the extension is proportional to the force*. Linear elastic behavior is an accurate model for small deformations of many materials.

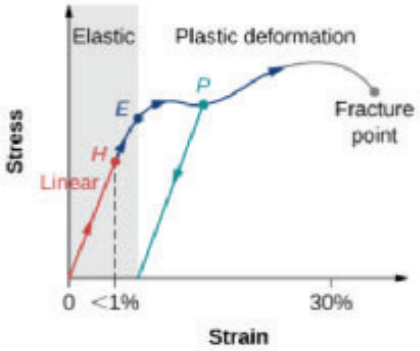

Figure 1: A typical stress-strain plot for a metal specimen. There is *linear elastic behavior* for displacements up to the point H: the limit of applicability of Hooke's law. There is *elastic behavior* up to the point E (the Elastic limit): unloading the specimen would return along the line from H to zero. Loading further induces *plastic behavior*: unloading the specimen from the point P to zero stress returns the specimen to a non-zero strain. Loading further eventually brings the specimen to the Fracture Point, and it breaks into parts: this is the *Ultimate Stress*.

The stress ϵ and the strain σ are each measured using three-dimensional tensors, and the linear relations between them are measured using fourth-order tensors:

$$\epsilon = \mathbb{S} \cdot \sigma \,; \quad \mathbb{S} \text{ is the linear-elastic stiffness fourth-order tensor;} \tag{1}$$

$$\sigma = C \cdot \epsilon \,; \quad \mathbb{C} \text{ is the linear-elastic compliance fourth-order tensor .} \tag{2}$$

Using cartesian components, this is expressed as:

$$\epsilon_{ij} = \Sigma_{mn} S_{ijmn} \sigma_{mn} \,; \tag{3}$$

$$\sigma_{ij} = \Sigma_{mn} C_{ijmn} \epsilon_{mn} \,. \tag{4}$$

When the relation is non-linear elastic, then the stiffness and compliance tensors become non-linear functions: in some cases, a power-series expansion has been useful. When the relation is plastic, then the stiffness and compliance become functions of the entire previous history of the strain, or stress, respectively.

The stiffness and compliance tensors are mathematical inverses of each other, and they usually are fields whose values depend on the location within the material. This is treated

in many texts on *Strength of Materials*.[6]

When the material's mechanical properties are uniform (i. e., homogeneous = independent of location within the material) and isotropic (i. e., independent of orientation of the material), then the structure of the stiffness and compliance tensors simplifies dramatically, to contain only two parameters, which are often chosen to be the bulk modulus B and the shear modulus G, or alternately, the Young's modulus E and the Poisson's ratio ν :

- The bulk modulus $B = -dp/d\ln(V)$ of a material is a measure of its resistance to compression, where p is the pressure applied to a specimen of the material, and V is the volume of the specimen.
- The shear modulus G = shear stress / shear strain = $(F/A)/(\Delta L/L)$ of a material is the measure of its resistance to an imposed shearing stress of a specimen of the material, where F is the transverse force applied to an area A at the top of a block of the material of height L, and ΔL is the transverse displacement of this area.
- The Young's modulus E = tensile stress / tensile strain = $(F/A)/(\Delta L/L)$ of a material is the measure of its resistance to an imposed tensile stress of a specimen of the material, where F is the tensile force applied to the top of a rod of the material of uniform cross sectional area A and length L, and ΔL is the extension of this rod. (Note the change in meaning of the quantities F, A, ΔL, and L in this definition, relative to the previous one.)
- The Poisson's ratio ν = − transverse strain / tensile strain of a material is a measure of the sideways contraction to the extension of a rod made of the material.

These parameters are inter-related such that any pair can be computed from a pair of the other parameters:

$$E = 2G(1+\nu) = 3B(1-2\nu) \quad (5)$$
$$G = (1/2)E/(1+\nu) = (3B/2)(1-2\nu)/(1+\nu) \quad (6)$$
$$B = (1/3)E/(1-2\nu) = (2G/3)(1+\nu)/(1-2\nu) \quad (7)$$
$$\nu = 1/2 - (1/6)(E/B) = (1/2)(E/G) - 1. \quad (8)$$

Many materials can usefully be modeled as *linear elastic*, and so the above substantial simplification of the full tensor equations is in wide use.

The crystal grains in the materials used in multi-layer ceramic capacitors do NOT have isotropic behaviors, either for their mechanical behaviors or for their electrical behaviors. One must be prepared to use the full tensor equations for both mechanical relations and for electrical relations. Also, there are substantial differences in properties between the materials of the primary grains and of the secondary (and tertiary, etc.) grains, and certainly

[6] One website discussing this is
`https://serc.carleton.edu/NAGTWorkshops/mineralogy/mineral_physics/tensors.html`

between the grains and pores; hence, the materials are NOT homogeneous at the level of the microstructure, and so one must be prepared to use the full tensor equations as position-dependent fields whose values depend on location, and not use elastic moduli as constants that apply uniformly to the entire dielectric of ceramic capacitors.

5 Fracture

Fracture is the separation of an object into two or more parts under the action of an applied stress. The fracture of the object usually happens when there is a crack[7] which the applied stress then extends throughout the object until the growing crack finally divides it. *Ductile fractures* happen after perceptible plastic deformation, while *brittle fractures* happen with little or no appreciable deformation, being characterized by rapid crack propagation with low energy release and without significant plastic deformation. The applied stress needed to create a fracture is called the *fracture strength* or the *breaking strength*, and is the object of *fracture mechanics*.

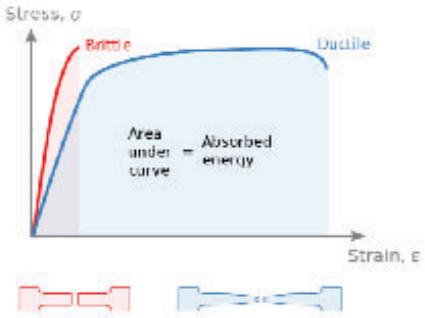

Figure 2: Two stress-strain plots, both showing linear elastic behavior for small strains, followed by dramatically different fracture behavior for larger strains. The brittle material fractures while still in the elastic region (but has exceeded the linear part of the elastic region), by the sudden growth of a crack traversing a cross section; the ductile material develops a plastic deformation including *neckdown*, until finally fracturing

A plot of the stress as strain increases differs dramatically for materials that are brittle relative to materials that are ductile, as do the appearances of dog-bone test specimens after fracture. Figure 2 shows the behavior of a brittle material, showing a linear elastic behavior for small strains, a non-linear elastic behavior for larger strains, and finally rupturing into two parts; it also shows the behavior of a ductile material, showing a long plastic extension

[7] The crack often starts at a surface of the object, but sometimes starts within the interior of the object. This crack is usually present before the application of the stress. A fractographic examination to identify the crack that initiates the fracture is well worthwhile!

before finally breaking. Also shown are typical examples of fractured dog-bone specimens, with the brittle fractured example showing negligible deformations, and the ductile fractured example showing substantial plastic deformations.

We are most concerned in this study with fracture; however, there can be confusion between *fracture toughness* and *hardness*, and the best way to deal with this is to be clear about the definition and measurement of each behavior. So I include discussion of both hardness and toughness.

6 Hardness

Hardness is the ability of a material to resist permanent deformation. (The deformation is not supposed to extend to fracture during testing.) It is measured by a test that examines the resistance to an indentation that is forced into the surface of a specimen of the material.

The most commonly used hardness tests are defined by the size and the shape and the material of the indenting tool used to induce the deformation, the size of the permanent deformation that results, and the amount of load applied to the tool.

The hardness numbers found by these tests are reported on an arbitrary scale, with increasing values representing harder surfaces. Many hardness tests have been studied, each one having a dedicated test machine producing its own unique hardness scale.

The *Brinell hardness test* was proposed by Swedish engineer Johan August Brinell in 1900. It was the first widely used, and standardized, hardness test in engineering and metallurgy. The typical test uses a 10 mm diameter steel ball as an indenter with a 29.42 kN (= 3,000 kgf) force pressed into the material for between 30 and 60 seconds. For softer materials, a smaller force is used; for harder materials, a tungsten carbide ball is substituted for the steel ball. When a steel ball is used, the Brinell hardness number is:

$$\text{BHN} = \frac{2P}{\pi D[D - \sqrt{D^2 - d^2}]} = \frac{2P}{\pi D^2[1 - \sqrt{1 - (D/d)^2}]}, \tag{9}$$

where P is the applied load in kilo-grams_force, D is the diameter of the indenter, and d is the diameter of indentation. (Note: When a tungsten carbide ball is used, replace "2" in the numerator by "0.102×2", and replace BHN by BHW.) The large size of indentation and possible damage to test-piece limits its usefulness. However, it also had the useful feature that the hardness value divided by two is roughly the approximate ultimate tensile strength (UTS) in ksi for steels. This feature contributed to its early adoption over others.

The *Rockwell hardness test* uses the permanent increase in the depth of indentation as a metric to measure hardness. The indenter is pressed on the surface, first with a minor load (98.1 N) and then with an additional load of increased magnitude within 2 to 8 seconds. The difference in the depth of penetration upon removal of the additional load is a measure of the hardness.

The *Knoop hardness test* is a micro-hardness test, used particularly for very brittle materials or thin sheets, where only a small indentation may be made. It was developed by Frederick Knoop and colleagues at the National Bureau of Standards (now NIST) of the United States in 1939, and is defined by the ASTM E384 standard. A pyramidal diamond point is pressed into the polished surface of the test material with a known load (often 100gf) for a specified dwell time, and the resulting indentation is measured using a microscope. The Knoop hardness HK or KHN is then given by the formula:

$$HK = \text{load (kgf) / [impression (area in sq-mm)]}. \tag{10}$$

The *Vickers hardness test* was developed in 1921 by Robert L. Smith and George E. Sandland at Vickers Ltd as an alternative to the Brinell method to measure the hardness of materials. The Vickers test is often easier to use than other hardness tests since the required calculations are independent of the size of the indenter, and the indenter can be used for all materials irrespective of hardness. The hardness number is determined by the load over the surface area of the indentation and not the area normal to the force, and is therefore not a pressure. The Vickers test has one of the widest scales among hardness tests. The unit of hardness given by the test is known as the Vickers Pyramid Number (HV) or Diamond Pyramid Hardness (DPH). The hardness number can be converted into units of pascals, but should not be confused with pressure, which uses the same units.

The *Shore hardness test*, the measurement device (called a durometer), and its use, were all developed by Albert Ferdinand Shore in the 1920s. The American Society for Testing and Material specification **ASTM D2240 Standard Test Method for Rubber Property – Durometer Hardness** (as of 2021) defines twelve different Shore durometer scales. The Shore durometer scales in most common use are Shore OO (for gels and for extremely soft rubbers), Shore A (harder materials such as rubbers and soft plastics), and Shore D (hardest plastics). Each of the Shore scales is nominal – numerical values provide a linear ranking in order of "least hard" (low Shore value) to "most hard" (large Shore value), but there is no absolute meaning to the values. A Shore durometer hardness test is carried out by forcing an indenter applied perpendicularly to the flat surface of the material into that surface, and measuring the depth of indentation: typically, this is 0.00 to 0.10 inches. Generally, a specimen should be at least 0.25 inches thick so that its back surface does not affect the penetration depth, and a specimen should extend sideways for 0.25 inches in each direction so the sides do not affect the penetration depth. Viscoelastic materials will show a steadily increasing penetration after initial loading, and so the elapsed interval between initial loading and final measurement of indentation must be recorded. The shape of the indenter and the applied force depend on the Shore scale. The Shore durometer hardness test usefully characterizes the indentation hardness of soft materials such as aerogels, gels, soft and medium-soft and hard plastics, various rubbers including vulcanized (thermoset) rubbers, leather, cellular materials (including corks and woods), and multi-element greases and waxes, among other materials.

Comment: The above hardness tests all involve poking a specimen made of the material-of-interest with a probe having a standardized shape, and measuring the extent of the de-

formation of the material. The specimen is supposed to deform, but not fracture.

The *Mohs scale of hardness* is an alternate, popular approach to the measurement of hardness, introduced in 1812 by the German geologist and mineralogist Friedrich Mohs. It is a qualitative ordinal scale, from 1 to 10, characterizing relative scratch resistance of various materials. Comparing the hardness of minerals by observing which can scratch others was mentioned by Theophrastus in his treatise *On Stones*, written about 300 BC, and by Pliny the Elder in his *Naturalis History*, written about AD 77. The Mohs scale is based on two observations:

1. Materials can be arranged into sets such that all the members of a given set can scratch each other: these have the same Mohs hardness.
2. These sets can be arranged in a line such that any member of a set can scratch any member of a set to the left, but no member from a set to the right: these sets are ordered from left to right in increasing Mohs hardness. (This is the meaning of *ordinal*.)

There is no accepted way to establish "distances" between these sets, and so it makes no sense to speak of one set as being "x times" as hard as another set. Rather, specific materials are chosen as landmarks on the scale: talc is assigned Mohs-1, and diamond is assigned Mohs-10. The Mohs scale has proven useful in milling operations such as used in the preparation of the powers used in ceramic capacitors; it allows an assessment of which kind of mill will best reduce a given product whose hardness is known. The Mohs hardness of the balls used in ball-mills, such as are used to mill the ceramics used in MLCC, is in the range from Mohs-6 to Mohs-9. (`https://www.powderprocess.net/Grinding_Milling.html`) The Mohs scale is used by electronic manufacturers for testing the resilience of flat panel display components (such as cover glass for LCDs or encapsulation for OLEDs), as well as to evaluate the hardness of touch screens in consumer electronics.

7 Fracture Toughness

Fracture toughness describes the resistance that a material offers to the lengthening of a crack under an applied stress, including cracks that grow enough to separate the specimens into distinct pieces: the fracture toughness is the *critical stress intensity factor* (defined below) for which propagation of the crack suddenly becomes rapid and unlimited; it is a property of the material, and of the *mode of loading* (also defined below). It is a central concept in linear elastic fracture mechanics (LEFM), whose roots date to about a century ago.

In 1911, Sir Charles Edward Inglis noted while studying the fracturing of the hulls of ships, that rivet holes often deformed from a circular shape into an elliptical one. He published in 1913 an exact stress-strain analysis in the context of linear elastic solid mechanics for a small elliptical hole in a large flat plate, showing that there is a magnification (intensification) of stress at and around the tip of an ellipse, and that this magnification grows without limit

as the crack thins: his work is the first serious mathematical analysis of the fracturing of materials.[8]

The first successful physical analysis of a fracture dominated problem was due to Alan Arnold Griffith in 1920, who considered the growth of cracks in a brittle material. Griffith formulated the now well-accepted concept that an existing crack will grow longer when the reduction in potential energy caused by the crack growth is greater than or equal to the increase in surface energy due to the creation of the new surface.[9] His theory allows the estimation of the theoretical strength (i. e., the strength when there are no cracks) of brittle materials and also gives the correct relationship between parameters controlling crack extension in brittle materials:

$$\sigma\sqrt{a} > \sqrt{2E\gamma/\pi} \tag{11}$$

where σ is the uniform stress applied to the specimen (fashioned as a plate) far from the crack and perpendicular to the long axis of the crack, $2a$ is the length of the crack, E is Young's modulus, and γ is the surface tension. Because the Young's modulus E and the surface tension γ are material properties, then the right hand side of this equation has a value that is characteristic of the particular material, provided that it is brittle. Crack extension happens when $\sigma\sqrt{a}$ exceeds this material constant.

Measuring the surface tension γ is difficult for most solids, but Griffith noted that γ could be measured for molten glass, and that the value for solid glass could be obtained by extrapolation, since there is no phase change in cooling to below the glass-transition temperature. He provided data that confirmed the relation between the parameters. Griffith used continuum linear elastic theory to relate stresses and strains near the tip of a crack, but noted that it is the microstructures, and their responses to stresses, that determines the critical conditions for fracture.

Generalizing his study to a large range of cracking geometries was the beginning of *linear elastic fracture mechanics* (LEFM).

An irony: *Griffith ingeniously studied glass because it allowed him to obtain reasonable experimental values for the surface tension of a solid. As part of his studies, he learned that the very low strength of glass specimens was caused by surface scratches, some down to atomic sizes: if these were prevented, then glass specimens became extremely strong. And he learned that cracking could be prevented by using a plastic to coat glass fibers immediately as they were drawn from the glass furnace: these coated glass fibers were immensely strong – this was the invention of fiberglass. However, his bosses were employing him to study how to make materials strong, and were outraged when they found that he was working on glass since they believed that it was well-known even to pre-schoolers that "glass was weak", so they transferred him to other work.*

[8] C. E. Inglis, *Stresses in a Plate Due to the Presence of Cracks and Sharp Corners*, Read at the Spring Meetings of the Fifty-fourth Session of the Institution of Naval Architects, March 14, 1913. The discussion following this paper is also remarkable.

C. E. Inglis, *Stresses in a Plate Due to the Presence of Cracks and Sharp Corners*, Transactions of the Institution of Naval Architects, Vol. 55, London, 1913, pages 219 to 230.

[9] A. A. Griffith, *The phenomena of rupture and flow in solids*, Philosophical Transactions of the Royal Society of London **A 221**, 163 to 198 (1921); Read before the Society in 1920.

When a single parameter uniquely describes the crack tip conditions, then the fracture toughness, which is a critical value of this parameter, is independent of specimen size, and depends only on the material and the environment. When the single-parameter assumption breaks down, fracture toughness becomes size dependent, and a small-scale fracture toughness test may not be indicative of the structural behavior. The load on a crack can span an enormous range of applied stress geometries but, in 1957, G. Irwin found any loading condition can be reduced to a combination of three fundamental modes of loading for extending a crack, giving three approaches to the measurement of fracture toughness:

- Mode I – Opening mode: a tensile stress acts normal to the plane of the crack,
- Mode II – Sliding mode: a shear stress acts parallel to the plane of the crack and perpendicular to the crack front, and,
- Mode III – Tearing mode: a shear stress acts parallel to the plane of the crack and parallel to the crack front.

For each of these three modes of loading, the form of the stress distribution around a crack tip, and close to it, is always the same. Computations of this stress distribution are available to relate the precise stress at the crack tip to the globally-applied loading for each mode for many geometries.

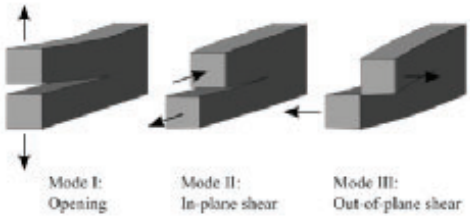

Figure 3: The three modes of opening. While there are three distinct modes of loading and also combinations of these three, it is Mode I loading that is most commonly studied.

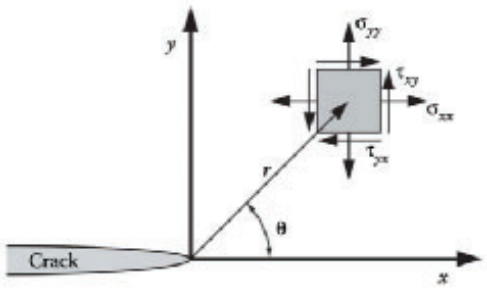

Figure 4: The x, y-coordinate system used for describing the stress field σ_{xx}, σ_{yy}, and τ_{xy}, τ_{yx} around the elliptically-shaped crack, shown touching the origin, and for a Mode I opening.

For example, for Mode I, for an elliptical crack of length $2a$ at the middle of a flat plate:

$$\sigma_{xx} = \left[K_I/\sqrt{2\pi r}\right]\cos(\theta/2)[1-\sin(\theta/2)\sin(3\theta/2)] \quad (12)$$

$$\sigma_{yy} = \left[K_I/\sqrt{2\pi r}\right]\cos(\theta/2)[1+\sin(\theta/2)\sin(3\theta/2)] \quad (13)$$

$$\tau_{xy}=\tau_{yx} = \left[K_I/\sqrt{2\pi r}\right]\cos(\theta/2)\sin(\theta/2)\cos(3\theta/2)] \quad (14)$$

where $K_I = \sigma\sqrt{\pi a}$ is the stress intensity factor for Mode I and where σ is the far-field stress (entirely parallel to the y-axis) and $2a$ is the length of the crack.

A different example: for Mode I and for an elliptical crack entering the edge of the flat plate for a distance of a, $K_I = 1.12\,\sigma\sqrt{\pi a}$; the 12% increase in the stress intensity factor relative to the first example is caused by different boundary conditions at the free edge of the flat plate, at the location of the entering crack.

Another example: a penny-shaped crack within a large block of material has $K_I = (2/\pi)\sigma\sqrt{\pi a}$ where a is the radius of the crack.

In order for this approach to be useful, one must be able to determine the stress intensity factor K from loads applied far from the crack, and from the geometry. Closed-form solutions for K have been derived for a number of simple configurations; three of these have been displayed above. For more complex situations, the stress intensity factor can be estimated by experiment or by numerical analysis. Several handbooks devoted solely to stress intensity solutions have been published:

- Tada, H., Paris, P. C., and Irwin, G. R., *The Stress Analysis of Cracks Handbook*, (2nd ed.). Paris Productions, Inc., St. Louis, 1985.
- Murakami, Y., *Stress Intensity Factors Handbook*, Pergamon Press, New York, 1987.
- Rooke, D. P. and Cartwright, D. J., *Compendium of Stress Intensity Factors*, Her Majesty's Stationary Office, London, 1976.

Thus, tests on a suitably shaped and loaded specimen (mode I, or mode II, or mode III), each with a pre-existing crack of a known length a, can be carried out to determine K. A number of organizations publish standards related to fracture toughness measurements, including ASTM (ASTM International, formerly known as American Society for Testing and Materials), BSI (British Standards Institution), ISO (International Organization for Standardization), and the Japan Society of Mechanical Engineers (JSME). See for example:

- ASTM C1161: Test Method for Flexural Strength of Advanced Ceramics at Ambient Temperature
- ASTM C1421: Standard Test Methods for Determination of Fracture Toughness of Advanced Ceramics at Ambient Temperature
- ASTM E399: Test Method for Plane-strain Fracture Toughness of Metallic Materials
- ASTM E740: Practice for Fracture Testing with Surface-Crack Tension Specimens
- ASTM E1820: Standard Test Method for Measurement of Fracture Toughness
- ASTM E1823: Terminology Relating to Fatigue and Fracture Testing
- ISO 12135: Metallic materials – Unified method of test for the determination of quasi-static fracture toughness
- ISO 28079:2009 – The Palmqvist method, used to determine the fracture toughness for cemented carbides

A key paper: J. A. Salem, G. D. Quinn, and M. G. Jenkins[10] discuss the results of three methods of measuring fracture toughness in connection with establishing the ASTM test method C1421. They focused on specimens of hot-pressed silicon nitride, fashioned into beams 3 mm by 4 mm by 45 mm. They measured fracture toughness using "surface crack in flexure", "single-edge pre-cracked beam", and "chevron notch in bending". They demonstrated that the mean fracture toughness for samples of five specimens concurred to within several percent regardless of which of the three test methods were used.

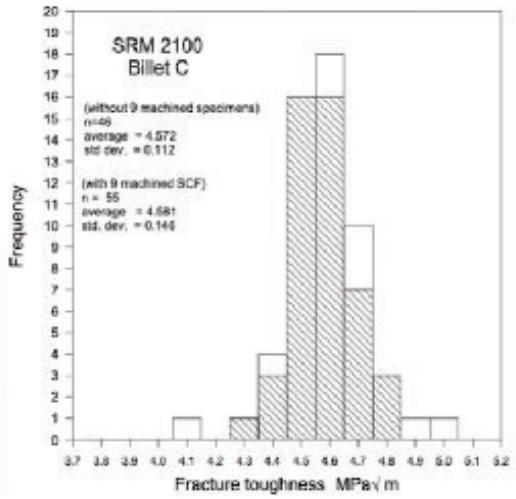

Figure 5: Histogram of values of Fracture Toughness of the NIST "Standard Reference Material" (SRM 2100), a version of Silicon Nitride. The cross-hatched bars are for 46 specimens with hand polished surfaces; the plain bars include 9 "Surface Crack in Flexure" (SCF) specimens with machined surfaces. (Note that the scale is expanded.) The variation of these data is ±2.4% for the hand polished specimens and ±3.2% for the ones with machined surfaces. That is, specimens with machined surfaces have a greater range of surface flaws than the hand polished ones.

8 Grain boundaries and toughness

The presence of grains in a material can affect its toughness by affecting the way cracks propagate. In front of a crack, the intensified stress can induce a plastic zone. Beyond that region, the material remains elastic. The conditions for fracture are the most favorable at the boundary between this plastic and elastic zone, and thus cracks often initiate by the cleavage of a grain at that location. At low temperatures, where the material can become completely brittle, such as in a body-centered cubic (BCC) metal, the plastic zone shrinks away, and only the elastic zone exists. In this state, the crack will propagate by successive cleavage of the grains. At these low temperatures, the yield strength is high, but the fracture strain and crack tip radius of curvature are low, leading to a low toughness. At higher temperatures, the yield strength decreases, and

[10] *Does anyone know the real fracture toughness? SRM 2100: The world's first ceramic toughness reference material*, pages 76 to 93 in Fracture Resistance Testing of Monolithic and Composite Brittle Materials, ASTM STP 1409 (2002)

leads to the formation of the plastic zone. Cleavage is likely to initiate at the elastic-plastic zone boundary, and then link back to the main crack tip. This is usually a mixture of cleavages of grains, and ductile fracture of grains known as fibrous linkages. The percentage of fibrous linkages increase as temperature increases until the linkup is entirely fibrous linkages. In this state, even though yield strength is lower, the presence of ductile fracture and a higher crack tip radius of curvature results in a higher toughness.

Grain-boundary strengthening, also called Hall-Petch strengthening, is a method of strengthening materials by changing their average crystallite (grain) size. It is based on the observation that grain boundaries are insurmountable borders for dislocations and that the number of dislocations within a grain has an effect on how stress builds up in the adjacent grain, which will eventually activate dislocation sources and thus enabling deformation in the neighbouring grain, too. So, by changing grain size one can influence the number of dislocations piled up at the grain boundary and yield strength.

The relation between yield stress and grain size is described mathematically by the Hall-Petch equation:

$$\sigma_{\text{yield}} = \sigma_0 + \frac{k_{\text{yield}}}{\sqrt{d}} \tag{15}$$

where σ_{yield} is the yield stress, σ_0 is a constant depending upon the material that relates to the stress needed to start movement of dislocations, k_{yield} is the material-dependent strengthening coefficient, and d is the average grain diameter. The Hall-Petch equation is often found to describe data over a wide range of grain diameters. It has been observed experimentally that the microstructure with the highest yield strength is a grain size of about 10 nm (3.9×10^{-7} in), because grains smaller than this undergo another yielding mechanism, *grain boundary sliding*.

However, the Hall-Petch equation does not always apply: there are complications in real materials that cause other relations than $1/\sqrt{d}$. One must make the measurements on the materials of interest to learn what is really true for that material.

9 Three studies demonstrating a relationship between fracture toughness K_{Ic} and grain size

K. M. Liang, G. Orange, and G. Fantozzi studied zirconia-toughened alumina composites with different compositions (0 to 100% ZrO_2), which gave materials with a wide range of elastic and fracture properties.[11] Specimens 4 mm by 3 mm by 20 mm were machined from sintered materials. The surfaces were polished successively with 6, 1 and finally 0.1 μm diamond pastes. After surface preparation, specimens were annealed (1,200°C for 15 minutes) to remove surface compressive stresses. Fracture toughness K_{Ic} was measured using the Standard Single Edge Notched Beam (SENB) technique, and also by the Direct Crack Measurement (DCM) based on the lengths of the cracks induced by a Vicker's indenter. The specimens were indented on the polished surface with a Vickers microhardness tester using loads ranging from 1 to 50 N, and with a Vickers hardness tester using loads from 100 to 500 N. Figure 6 shows the consistency of their measured values of fracture toughness K_{Ic} with various conditions of measurement, over a range of concentrations of Zirconia, and Figure 7 shows that values of fracture toughness K_{Ic} are a function of grain size Φ over the range 2 to 12 μm.

F. Buresch measured the fracture toughness of two specimens of alumina, and found a direct relationship to grain sizes between about 1 and 4 μm.[12] See Figure 8.

[11] *Evaluation by indentation of fracture toughness of ceramic materials*, **Journal of Materials Science**, **25** (1990) pages 207 to 214.

[12] "A Structure Sensitive K_{Ic}-value and its Dependence on Grain Size Distribution, Density and Microcrack Interaction", by Friedrich El Buresch. From *Fracture Mechanics of Ceramics: Volume 4: Crack Growth and*

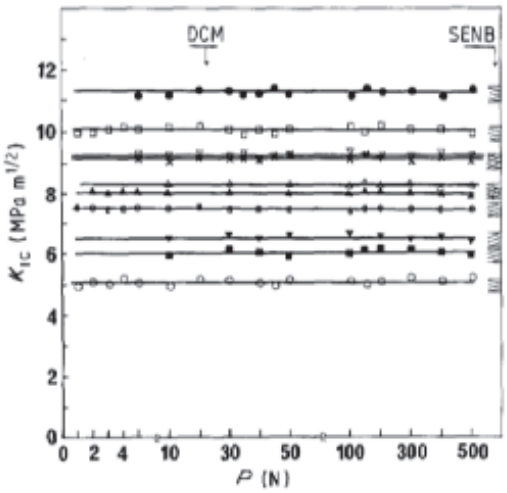

Figure 8 Comparison of fracture toughness values of Al_2O_3–ZrO_2 using Equation 21 with that measured by SENB. (○) Al_2O_3, (▲) A5Z0Y, (□) A10Z0Y, (▼) A15Z0Y, (■) A20Z0Y, (△) A20Z1Y, (×) A20Z2Y, (e) A20Z3Y, (△) A45Z3Y, (●) TZP.

Figure 6: From the publication of Lang, et al. showing two things: (1) the fracture toughness values K_{Ic} obtained by the Direct Crack Measurement (DCM) method do not change with the load P over the range 1 N to 500 N, and (2) these values are essentially the same whether determined using DCM or by using the Standard Single Edge Notched Beam (SENB) technique. (The SENB measurements are crowded against the right-hand side of this plot.)

M. Trunec studied the dependence of mechanical properties of yttria-stabilized tetragonal zirconia ceramic polycrystals with 3 mol% Y_2O_3 (3Y-TZP) on grain sizes ranging from 0.19 μm to 2.15 μm.[13] For comparison, a nanocrystalline zirconia powder B261 was also measured. Vickers indentation tests were used to determine hardness and fracture toughness. The hardness decreased with increasing grain size, while the fracture toughness increased. Both 3Y-TZP and B261 showed essentially the same values of fracture toughness versus grain size over the tested range. See Figure 9.

10 Inclusions

Inclusions in a material (such as particles of a second phase) can act similar to brittle grains, and thus can affect crack propagation. Fracture or de-cohesion at the inclusion can either be caused by the external applied stress or by the dislocations generated by the requirement of the inclusion to maintain contiguity with the matrix around it. Similar to grains, the fracture is most likely to occur at the plastic-elastic zone boundary. Then the crack can linkup back to the main crack. If the plastic zone is small or the density of

Microstructure, edited by R. C. Bradt, D. P. H. Hasselman, and F. F. Lange. Plenum Press, 1973.

[13] *Ceramics-Silikaty* 52 (3) pages 165 to 171 (2008).

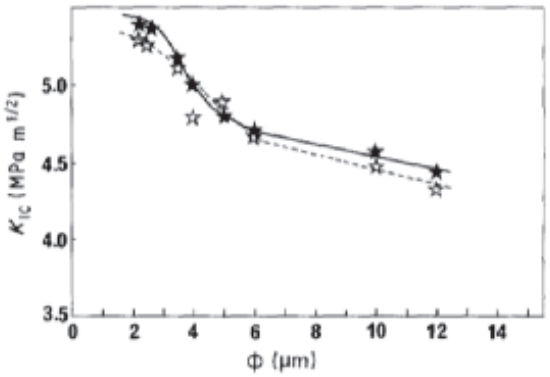

Figure 10 Comparison of fracture toughness values of pure alumina of different grain sizes calculated by (★) DCM using Equation 21 with that determined by (☆) SENB.

Figure 7: From the publication of Lang, et al. showing two things: (1) the fracture toughness values K_{Ic} of pure aluminia measured using DCM are substantially the same as those measured using SENB, for average grain sizes ϕ ranging from 2 μm to 12 μm, and (2) the fracture toughness values K_{Ic} are a well-defined function of the average grain size ϕ from 2 μm to 12 μm.

the inclusions is small, the fracture is more likely to directly link up with the main crack tip. If the plastic zone is large, or the density of inclusions is high, additional inclusion fractures may occur within the plastic zone, and linkup occurs by progressing from the crack to the closest fracturing inclusion within the zone.

11 Conclusions

Ceramics are brittle: they are prone to crack under small stresses, and show no pre-cursing deformation: the cracking of MLCCs has harmed a number of NASA projects. Their strength against fracture can be characterized by a material parameter, the *critical fracture toughness* K_c, which depends on the cracking mode, I or II or III; however, mode I cracking, and therefore K_{Ic} is most descriptive for MLCC cracking.

The best policy would be to make direct measurement of K_{Ic} on MLCCs; however, no one has developed reliable methods for doing this. One problem is that the units are physically small. Another is that the electrodes and wraparound end terminations, which are ductile metals and are a substantial fraction of the MLCC, complicate the stressing of the ceramic layers: unravelling these interactions has not yet been done, and may never be done.

Grain size distributions affect the value of K_{Ic}, and therefore can be a proxy for it: one can imagine comparing different production lots of capacitors by comparing the distributions of their grain sizes.

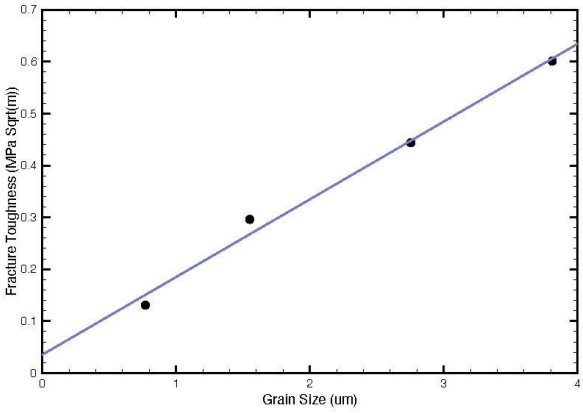

Figure 8: From the publication of F. Buresch, showing the fracture toughness values K_{Ic} for two specimens of alumina as a function of grain size from about 1 μm to about 4 μm.

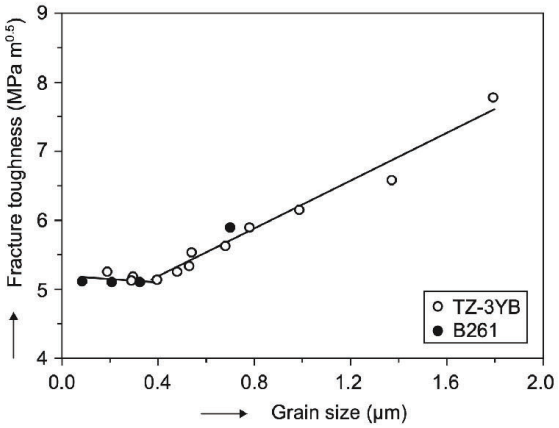

Figure 9: From the publication of M. Trunec, showing that the fracture toughness values K_{Ic} for both TZ-3YB and B261 depended on their grain size, from about 0.1 μm to 1.7 μm, in the same way.

From:	Baughman, James M. (LARC-D307)[TEAMS3]
To:	Moran, Erin (LARC-C101)[TEAMS3]
Subject:	RE: SIGNATURE CHECK: NESC Ceramic Capacitor Grain Size Analysis Using Electron Backscatter Diffraction (EBSD) Report
Date:	Thursday, February 23, 2023 7:18:43 PM

I am sending this to you with this statement
"I have read the subject NESC report and this email will suffice as my concurrence and signature since I do not have the capability to digitally sign this report."
James M Baughman

From: Moran, Erin (LARC-C101)[TEAMS3] <erin.moran-1@nasa.gov>
Sent: Tuesday, February 21, 2023 9:27 AM
To: Tayon, Wesley A. (LARC-D307) <wesley.a.tayon@nasa.gov>; Baughman, James M. (LARC-D307)[TEAMS3] <james.m.baughman@nasa.gov>
Cc: Douglas, Susana P. (GSFC-5000) <susana.p.douglas@nasa.gov>; Hodson, Robert F. (LARC-C104) <robert.f.hodson@nasa.gov>
Subject: SIGNATURE CHECK: NESC Ceramic Capacitor Grain Size Analysis Using Electron Backscatter Diffraction (EBSD) Report

Good Morning Wes and Jim,
The subject NESC report was approved at the February 16, 2023, NRB and will be uploaded to the NESC configuration control site. Bob requested you as a signee on the subject final report. Before I prepare the final pdf version (config control process) with signature tabs (locks the pdf), I'm checking to see if you both have the capability to digitally sign.
If you are unable to sign digitally, please reply to this email with below statement. Then, I'll insert Electronic Signature received on the Signature page. Thanks!
Susana/Bob: Then, I'll prepare the report for the rest of signatures.

"I have read the subject NESC report and this email will suffice as my concurrence and signature since I do not have the capability to digitally sign this report."

Thanks!

Erin Moran
TEAMS 3 Supervisor for Project Coordination, NASA Engineering and Safety Center (NESC)
Technical Writer/Editor
NASA LaRC Bldg.1219, MS 107
11 Langley Blvd, Hampton, VA 23681

Analytical Mechanics Associates
t. ~~757.864.7513~~
f.. 757.864.6601
e.. erin.moran-1@nasa.gov
e. erin.moran@ama-inc.com
w. www.ama-inc.com
a. 21 Enterprise Parkway, Suite 300, Hampton, VA 23666

REPORT DOCUMENTATION PAGE

Form Approved
OMB No. 0704-0188

The public reporting burden for this collection of information is estimated to average 1 hour per response, including the time for reviewing instructions, searching existing data sources, gathering and maintaining the data needed, and completing and reviewing the collection of information. Send comments regarding this burden estimate or any other aspect of this collection of information, including suggestions for reducing the burden, to Department of Defense, Washington Headquarters Services, Directorate for Information Operations and Reports (0704-0188), 1215 Jefferson Davis Highway, Suite 1204, Arlington, VA 22202-4302. Respondents should be aware that notwithstanding any other provision of law, no person shall be subject to any penalty for failing to comply with a collection of information if it does not display a currently valid OMB control number.
PLEASE DO NOT RETURN YOUR FORM TO THE ABOVE ADDRESS.

1. REPORT DATE *(DD-MM-YYYY)*	2. REPORT TYPE	3. DATES COVERED *(From - To)*
03/29/2023	Technical Memorandum	

4. TITLE AND SUBTITLE
Ceramic Capacitor Grain Size Analysis Using Electron Backscatter Diffraction (EBSD)

5a. CONTRACT NUMBER

5b. GRANT NUMBER

5c. PROGRAM ELEMENT NUMBER

6. AUTHOR(S)
Hodson, Robert F.; Douglas, Susana P.; Green, Christopher M.; Tayon, Wesley A.; Baughman, James M.; Brusse, Jay A.; Leidecker, Henning W.

5d. PROJECT NUMBER

5e. TASK NUMBER

5f. WORK UNIT NUMBER
869021.01.23.01.01

7. PERFORMING ORGANIZATION NAME(S) AND ADDRESS(ES)
NASA Langley Research Center
Hampton, VA 23681-2199

8. PERFORMING ORGANIZATION REPORT NUMBER
NESC-RP-19-01418

9. SPONSORING/MONITORING AGENCY NAME(S) AND ADDRESS(ES)
National Aeronautics and Space Administration
Washington, DC 20546-0001

10. SPONSOR/MONITOR'S ACRONYM(S)
NASA

11. SPONSOR/MONITOR'S REPORT NUMBER(S)
NASA/TM-20230004147

12. DISTRIBUTION/AVAILABILITY STATEMENT
Unclassified - Unlimited
Subject Category Electronics and Electrical Engineering
Availability: NASA STI Program (757) 864-9658

13. SUPPLEMENTARY NOTES

14. ABSTRACT
The overall scope of this NESC study was to identify (or develop) a tool, methodology, or process that can inspect a ceramic capacitor and consistently return repeatable grain size distribution results. It is important to note that the development of a machine learning technique was considered as an option for this study, but only if an existing automated tool was not available. This report explains why the Electron Backscatter Diffraction analysis method for grain structure and size distribution was deemed a suitable candidate for this work.

15. SUBJECT TERMS
Electron Backscatter Diffraction; Automated Tool; Machine Leaning; Multilayer Ceramic Capacitors; NASA Engineering and Safety Center

16. SECURITY CLASSIFICATION OF:			17. LIMITATION OF ABSTRACT	18. NUMBER OF PAGES	19a. NAME OF RESPONSIBLE PERSON
a. REPORT	b. ABSTRACT	c. THIS PAGE			STI Help Desk (email: help@sti.nasa.gov)
					19b. TELEPHONE NUMBER *(Include area code)*
U	U	U	UU	60	(443) 757-5802